PREPARED FOR SUBMISSION TO JCAP

arXiv:1905.08890v1 [astro-ph.CO] 21 May 2019

# GRAMSES: a new route to general relativistic $N$-body simulations in cosmology - I. Methodology and code description

**Cristian Barrera-Hinojosa**[a] **and Baojiu Li**[a]

[a]Institute for Computational Cosmology, Department of Physics, Durham University,
Durham DH1 3LE, UK

E-mail: cristian.g.barrera@durham.ac.uk, baojiu.li@durham.ac.uk

**Abstract.** We present GRAMSES, a new pipeline for nonlinear cosmological $N$-body simulations in General Relativity (GR). This code adopts the Arnowitt-Deser-Misner (ADM) formalism of GR, with constant mean curvature and minimum distortion gauge fixings, which provides a fully nonlinear and background independent framework for relativistic cosmology. Employing the fully constrained formulation, the Einstein equation is reduced to a set of ten elliptical equations solved using multigrid relaxation on adaptive mesh refinements (AMR), and three hyperbolic equations for the evolution of dynamical degrees of freedom. The current version of GRAMSES neglects the evolution equations for the gravitational sector by using the conformal flatness approximation, which allows it to compute the two scalar and two vector degrees of freedom, while extensions to include these evolution equations are ongoing. In this paper we describe the methodology, implementation, code tests and first results for cosmological simulations in a $\Lambda$CDM universe, while the generation of initial conditions and physical results will be discussed elsewhere. Inheriting the efficient AMR and massive parallelisation infrastructure from the publicly-available $N$-body and hydrodynamic simulation code RAMSES, GRAMSES is ideal for studying the detailed behaviour of spacetime inside virialised cosmic structures and hence accurately quantifying the impact of backreaction effects on the cosmic expansion, as well as for investigating GR effects on cosmological observables using cosmic-volume simulations.

## Contents

## 1 Introduction

The challenge of implementing cosmological simulations based on General Relativity (GR) for studying structure formation in our Universe has received increasing attention in the last few years, not only as a more accurate counterpart to Newtonian simulations in the era of precision cosmology, but also as a natural framework to study phenomena beyond the Newtonian approximation. Large upcoming surveys, such as LSST [1], Euclid [2] and DESI [3], aim at mapping billions of galaxies with unprecedented precision and will open up the possibility of detecting new general relativistic effects in cosmological observables, whose precise modelling might require a new generation of cosmological simulations based on GR. As an example, the long-standing issue of the back-reaction effect [4], i.e., the impact of matter inhomogeneities on the cosmic expansion rate, requires a unified GR treatment for spacetime and matter. While the Newtonian approximation offers an intuitive description for gravity, and simulations based on it enjoy a remarkable success in explaining the observable Universe so far [5–7], the assumption of a Friedmann-Lemaître-Robertson-Walker (FLRW) background turns the Hubble parameter into an external input that is dissociated from the structure formation process that might take place. Furthermore, attempts to include this back-reaction in Newtonian simulations result in null contributions by construction [8–10]. Even if back-reaction may not fulfill its original purpose of explaining the observed accelerated cosmic expansion, it can still contribute to our understanding of dark energy and possibly to alleviate the current $3\sigma$ tension between the Hubble constant determination from the local [11] and distant [12] Universe. Recent attempts to study back-reaction effects in a GR framework show that local deviations from the average expansion rate of the Universe can be substantial in underdense regions [13] and might impact our estimation of cosmological parameters in a $\Lambda$CDM model even at the percent level [14]. In any case, a fully non-linear, general relativistic framework is needed in order to reach conclusive answers to this problem in the late-time Universe.

The rise of modern $N$-body cosmological simulations taking a leap beyond the Newtonian approximation was first achieved by the GEVOLUTION code [15–20]. This is based on a weak-field expansion around a FLRW background, which allows to linearise the equations for the gravitational sector while keeping the nonlinearities in the energy-momentum tensor, whose components become 'dressed' by the weakly perturbed metric. Following the standards set by state-of-the-art Newtonian simulations, in GEVOLUTION the dark matter content of the Universe is described as a particle ensemble, which allow to track them even after trajectory-crossing occurs. The latter is crucial to get a realistic structure formation history since such phenomenon appears in the formation of virialised dark matter haloes.

Another interesting path for implementing general relativistic cosmological simulations is to resort to numerical relativity which condenses the theoretical and numerical tools needed for modelling relativistic systems. Even if the first applications of numerical relativity to study cosmological spacetimes were explored during the 80's [21], modern developments in this direction arguably started with the COSMOGRAPH code [22] and the work of Betivegna & Bruni [13], followed by that of Macpherson *et al.* [23]. Some of these GR codes based on numerical relativity share a common feature of being developed upon the Einstein Toolkit [24], an open-source community infrastructure for relativistic astrophysics. These implement the Baumgarte-Shapiro-Shibata-Nakamura (BSSN) formulation for a numerically stable spacetime evolution [25–27] – one of the cornerstones in modern numerical relativity – and general relativistic hydrodynamics for the matter sector. This latter aspect, however, is different from standard cosmological simulations and the approximation of treating dark matter as a fluid means that particle trajectories after shell crossing in bound structures are not exactly followed during the simulation. For instance, a comparison of fully non-linear GR simulations with pressureless dark matter fluid and Newtonian $N$-body simulations shows partial discrepancies inside the (Newtonian) dark matter haloes where the weak field condition is violated [28], but the different treatments for matter make the results difficult to assess and demands a fully GR $N$-body simulation. More recently, Daverio *et al.* [29] has made an attempt in this direction, by implementing full GR solutions in an $N$-body system.

In this paper we introduce a new code, GRAMSES, which combines the advantages of the above state-of-the-art GR cosmological codes while also adding new features specially relevant for structure formation simulations. Based on the Arnowitt-Deser-Misner (ADM) formalism [30], it implements a fully non-linear and background-independent set of elliptic-type partial differential equations (PDEs) for the gravitational sector which are solved using multigrid Gauss-Seidel relaxation. Meanwhile, GRAMSES offers an $N$-body description for non-relativistic dark matter particles, as well as supporting adaptive mesh refinement (AMR) to increase force resolution in high-density regions, so that the cosmic web formed in the simulations can be resolved to a high degree of details even after shell crossing. Our code is based on the publicly-available $N$-body and hydrodynamical simulation code

RAMSES [31], which is efficiently parallelised using Message Passing Interface (MPI). Particles are evolved along geodesics using a leapfrog method, and the particle-to-mesh projection and force interpolation is performed in a Cloud-In-Cell (CIC) scheme.

In order to deal with the nonlinear general relativistic equations for the gravitational sector in an optimal way for cosmology, GRAMSES implements the so-called fully constrained formulation (FCF) of GR [32, 33]. It is well known that the evolution equations for the gravitational sector in the ADM formalism are only weakly-hyperbolic and hence numerically unstable [34], a problem that is fixed by the BSSN formalism with the introduction of additional dynamical variables. However, assuming that gravitational waves (GW, which are the only dynamical degrees of freedom in GR) do not play a significant role in the cosmological dynamics and its back-reaction on the spacetime, we can neglect these so that time evolution is only due to the matter sector. This is very much in the similar spirit as the 'waveless theories of gravity' developed by Isenberg [35] and latter by Wilson & Mathews [36], who sought the natural generalisation of Newtonian gravity within GR. Then, in the resulting formulation only elliptic-type equations are solved to reconstruct the spacetime in absence of gravitational waves [37] and particles are evolved along geodesics. We stress, however, that this 'waveless approximation' does not constitute a fundamental limitation of GRAMSES, as gravitational waves can still be implemented in the simulations [38] straightforwardly, a task which will be left for future work.

The rest of the paper is organised as follows. In Section 2 we introduce the equations for the gravitational sector in the fully constrained ADM formulation of GR, while in Section 3 we describe the matter sector. In Section 4 we discuss the code structure and the numerical implementations of the GR equations in GRAMSES. In Section 5 we show some test results for the calculation of the relativistic source terms as well as for the multigrid solvers. Finally, in Section 6 we present some first results for cosmological simulations in a $\Lambda$CDM universe, although the generation of initial conditions and physical implications will be addressed in subsequent papers.

Throughout this paper we adopt the $(-,+,+,+)$ signature for the spacetime metric. Geometric units, where $G = c = 1$, are used in the theory part of the paper for brevity, but this are restored in Section 4 in order to introduce code units (which are used in the actual equations solved in GRAMSES). Greek indices run from 0 to 3, whereas Latin ones from 1 to 3 only, with repeated indices implying summation.

## 2 Field equations for the gravitational sector

In this section we review some fundamental aspects of numerical relativity that are at the core of this work. For a comprehensive discussion on these topics we refer the reader to [39–41].

### 2.1 The Arnowitt-Deser-Misner formalism

In the ADM (3+1) formalism [30], the 4-dimensional spacetime is foliated into 3-dimensional hypersurfaces of constant times characterised by some unit vector $n^\mu$, with which we can write a set of evolution and constraint equations for the variables $(\gamma_{ij}, K_{ij})$, representing the (induced) spatial metric of the 3-dimensional embedded manifold and its extrinsic curvature, respectively. The spacetime metric in the ADM formalism is given by

$$ds^2 = g_{\mu\nu}dx^\mu dx^\nu = -\alpha^2 dt^2 + \gamma_{ij}(\beta^i dt + dx^i)(\beta^j dt + dx^j), \tag{2.1}$$

in which the lapse function $\alpha$ and shift vector $\beta^i$ represent gauge (or coordinate) degrees of freedom. The projection of the Einstein equations into the 3-dimensional hypersurfaces yields the Hamiltonian constraint and the momentum constraint, respectively given by

$$R + K^2 - K_{ij}K^{ij} = 16\pi\rho \,, \tag{2.2}$$

$$D_j(K^{ij} - \gamma^{ij}K) = 8\pi S^i \,, \tag{2.3}$$

where $K = \gamma^{ij}K_{ij}$ is the trace of the extrinsic curvature, $D_i$ the covariant derivative associated with the spatial metric $\gamma_{ij}$ and $R$ the Ricci scalar. Here, we have introduced the energy density $\rho$ and the momentum density $S_i$ measured by a normal observer $n^\mu$, which are calculated by projecting the energy-momentum tensor as

$$\rho \equiv n_\mu n_\nu T^{\mu\nu} \,, \tag{2.4}$$

$$S_i \equiv -\gamma_{i\mu} n_\nu T^{\mu\nu} \,, \tag{2.5}$$

where $n_\mu = (-\alpha, 0)$. In addition to the constraint equations (2.2) and (2.3), which offer no dynamics, the evolution equations for $(\gamma_{ij}, K_{ij})$ are

$$(\partial_t - \mathcal{L}_\beta)\gamma_{ij} = -\,2\alpha K_{ij} \,, \tag{2.6}$$

$$(\partial_t - \mathcal{L}_\beta)K_{ij} = -\,D_iD_j\alpha + \alpha(R_{ij} - 2K_{ik}K^k_j + KK_{ij}) - 8\pi\alpha\left[S_{ij} - \frac{1}{2}\gamma_{ij}(S-\rho)\right] \,, \tag{2.7}$$

where

$$\mathcal{L}_\beta\gamma_{ij} = D_i\beta_j + D_j\beta_i \,, \tag{2.8}$$

and

$$\mathcal{L}_\beta K_{ij} = \beta^k\partial_k K_{ij} + K_{ik}\partial_j\beta^k + K_{kj}\partial_i\beta^k \,, \tag{2.9}$$

correspond to Lie derivatives along $\beta^i$. In addition to the matter source terms (2.4) and (2.5), in Eq. (2.7) we have defined the spatial stress $S_{ij} \equiv \gamma_{i\mu}\gamma_{j\nu}T^{\mu\nu}$, with $S = \gamma^{ij}S_{ij}$ its trace.

In order to disentangle the physical and gauge degrees of freedom at the nonlinear level we can resort to decompose $(\gamma_{ij}, K_{ij})$. As a method to single out a particular degree of freedom in the spatial metric $\gamma_{ij}$, we use the conformal transformation [42]

$$\gamma_{ij} = \psi^4\bar{\gamma}_{ij}, \tag{2.10}$$

where $\psi = \gamma^{1/3}$ is the conformal factor, $\bar{\gamma}_{ij}$ the conformal metric, and $\gamma \equiv \det{(\gamma_{ij})}$ the determinant of the metric $\gamma_{ij}$. We also introduce a conformal transformation for the traceless part of the extrinsic curvature $A_{ij} \equiv K_{ij} - \gamma_{ij}K/3$ as

$$A^{ij} = \psi^{-10}\bar{A}^{ij} \,.$$

Notice that for raising and lowering indices of the conformal (overbarred) quantities we use $\bar{\gamma}^{ij}$ and $\bar{\gamma}_{ij}$, respectively. Then, the Hamiltonian (2.2) and momentum (2.3) constraints can be rewritten as

$$8\bar{D}^2\psi - \psi\bar{R} - \frac{2}{3}\psi^5K^2 + \psi^{-7}\bar{A}_{ij}\bar{A}^{ij} = -16\pi\psi^5\rho \,, \tag{2.11}$$

$$\bar{D}_j\bar{A}^{ij} - \frac{2}{3}\psi^6\bar{\gamma}^{ij}\bar{D}_jK = 8\pi\psi^{10}S^i \,. \tag{2.12}$$

## 2.2 The conformal transverse traceless decomposition

By applying the Conformal Transverse Traceless (CTT) decomposition [43] (also known as York-Lichnerowicz formulation), we can further isolate degrees of freedom in the extrinsic curvature by decomposing the traceless, symmetric tensor $\bar{A}^{ij}$ into a transverse-traceless (TT) part which is divergenceless, and a longitudinal part that is written in terms as the vector gradient of a vector potential, namely

$$\bar{A}^{ij} = \bar{A}^{ij}_{TT} + \bar{A}^{ij}_{L} \,, \tag{2.13}$$

with $\bar{D}_j \bar{A}^{ij}_{TT} = 0$ and

$$\bar{A}^{ij}_{L} = \bar{D}^i W^j + \bar{D}^j W^i - \frac{2}{3}\bar{\gamma}^{ij}\bar{D}_k W^k \equiv (\bar{L}W)^{ij} \,, \tag{2.14}$$

where $W^j$ can be regarded as a vector potential and $\bar{L}$ is the longitudinal operator (also known as vector gradient or conformal Killing operator). Then, the momentum constraint (2.12) can be written in terms of the vector potential as

$$(\bar{\Delta}_L W)_i - \frac{2}{3}\psi^6 \bar{D}_i K = 8\pi\psi^6 S_i \,, \tag{2.15}$$

where $(\bar{\Delta}_L W)^i \equiv \bar{D}_j \bar{A}^{ij}$ is the vector Laplacian, and we have used that $\bar{\gamma}_{ij}\bar{\gamma}^{jk} = \delta^k_i$. A convenient feature about the previous equation is that we can decouple it from the rest in some particular cases, e.g., if we take $K = 0$ (a maximal slicing) and identify the conformal source term as

$$s_i \equiv \psi^6 S_i. \tag{2.16}$$

Notice that the TT part of $\bar{A}^{ij}$ is not constrained by (2.15); in fact $\bar{A}^{ij}_{TT}$ are dynamical degrees of freedom connected with gravitational waves. Then, if we want to find a solution in the absence of GW for a given 3-dimensional hypersurface at $t = t_0$ we might take $\bar{A}^{ij}_{TT} = 0$, but since this is a dynamical quantity, we do not have the freedom to fix this again at a $t > t_0$ time slice but we would need to solve the evolution equations to propagate them. We will come back to this point in the next section when we introduce the 'waveless approximation'.

## 2.3 Gauge fixing

As discussed in the previous subsection, the conformal decomposition and the CTT approach recast the constraint equations in a convenient form without any assumption about the way that the system evolves, and then the lapse function $\alpha$ and shift vector $\beta^i$ remain completely unspecified. Even if we have complete freedom to choose them as they correspond to picking a coordinate system, in practice not all options are physically or numerically convenient. For instance, the simplest option $\alpha = 1$ and $\beta^i = 0$, known as geodesic slicing (or synchronous gauge) is not always suitable since coordinates can become ill-defined at some point during the evolution of the system, e.g., when shell crossing (or orbit crossing) occurs, as it is expected for collisionless particles.

In order to study cosmological (i.e., expanding/contracting) spacetimes, a convenient prescription to choose $\alpha$ is by applying the so-called Constant Mean Curvature (CMC) slicing condition [44], in which we can set

$$K = -3H(t) \,, \tag{2.17}$$

where a fiducial Hubble parameter $H \equiv \dot{a}/a$ has been introduced (being $a$ a fiducial scale factor). Then, the lapse function can be found by solving the following constraint arising from (2.2) and the trace of (2.7) in terms of conformal variables,

$$\bar{D}^2(\alpha\psi) = \alpha\psi\left[\frac{7}{8}\psi^{-8}\bar{A}_{ij}\bar{A}^{ij} + \frac{5}{12}\psi^4 K^2 + \frac{1}{8}\bar{R} + 2\pi\psi^4(\rho + 2S)\right] - \psi^5 \dot{K} \,. \tag{2.18}$$

Notice that in this scheme $H$ (or $a$) is just a prescribed function for fixing the gauge, and in principle does not represent average (or background) properties of the universe. Nonetheless, we can still fix it by demanding that this satisfy the 'reference' (or 'background') Friedmann equations

$$H^2 = \frac{8\pi}{3}(\hat{\rho}_m + \rho_\Lambda)\,, \tag{2.19}$$

$$H^2 + \dot{H} = -4\pi(\hat{\rho}_m + \rho_\Lambda + 3\hat{P})\,, \tag{2.20}$$

where $\hat{\rho}_m$ and $\rho_\Lambda$ are the homogeneous[1] matter and dark energy densities in the reference spacetime, respectively, and $\hat{P} = \hat{S}/3$. The advantage of introducing the fiducial Friedmann equations (2.19) and (2.20) is that we can subtract 'background' quantities from the full GR equations, which is more numerically convenient than to solve them directly. A similar idea is also exploited in [45], where a reference FLRW spacetime is conveniently subtracted (but under geodesic slicing), and the application of a fiducial Hubble parameter as part of the CMC slicing condition is later considered in [46]. We remark that, on itself, this 'background' subtraction does not constitute an approximation nor a perturbative approach, but rather it is simply a reformulation of the equations using a cosmologically motivated slicing condition.

On the other hand, to fix the remaining gauge freedom let us consider the Minimal Distortion (MD) condition, in which $\beta^i$ is chosen such that it minimises the time rate of change of $\bar{\gamma}_{ij}$ during the propagation of spatial coordinates from one hypersurface to the next one. From the traceless part of (2.6) in terms of conformal quantities, we find

$$\bar{A}^{ij} = \frac{\psi^6}{2\alpha}\left[(\bar{L}\beta)^{ij} + \partial_t\bar{\gamma}^{ij}\right]\,, \tag{2.21}$$

and the MD condition corresponds to demand [44, 47]

$$D^i(\gamma^{1/3}\partial_t\bar{\gamma}_{ij}) = 0\,. \tag{2.22}$$

Let us remark here that, contrary to the decomposition (2.14) discussed in the CTT approach, in (2.21) $\bar{A}^{ij}$ has both longitudinal and transverse components even when the MD condition (2.22) is satisfied. Then, using the MD condition (2.22) the momentum constraint (2.12) translates into the following elliptic equation for the shift vector

$$(\bar{\Delta}_L\beta)^i + (\bar{L}\beta)^{ij}\bar{D}_j\ln\psi^6 = 2\psi^{-6}\bar{A}^{ij}\bar{D}_j\alpha + 16\pi\psi^4\alpha S^i, \tag{2.23}$$

where we have also used the CMC condition to simplify the momentum constraint. In the rest of the paper the gauge is fixed by the MD condition and the CMC condition, so that (2.17), (2.18) and (2.23) are satisfied, although the latter is simplified by the approximation introduced in the next subsection. In addition, we use the reference FLRW equations (2.19) and (2.20) to determine $K$ and $\dot{K}$.

## 2.4 The fully constrained formulation of GR

One of the fingerprints of GR is that gravity is no longer a static field as in Newton's theory, where the gravitational potential $\Phi_N$ is completely 'slaved' by the matter distribution, but it hosts two dynamical degrees of freedom representing ripples in the spacetime. Due to their faint nature, the existence of these GW has been only recently confirmed by LIGO [48, 49] – about a century after

---

[1] Note that we use an overhat to denote the homogeneous matter quantities in order to avoid confusion with the overbars used above to denote geometric quantities constructed from the conformal metric $\bar{\gamma}_{ij}$. For $\rho_\Lambda$, on the other hand, we omit the overhat for brevity because it does not have an inhomogeneous part.

its theoretical prediction [50] – and has opened up a plethora of new possibilities for exploring our Universe. However, in the context of cosmological structure formation and its back-reaction these play a subdominant role, and then one might try to reconstruct the spacetime in absence of GW while retaining all other virtues of GR. Therefore, as a natural extension of Newtonian $N$-body simulations, we propose to use a formulation of GR featuring only elliptic equations as a first step.

In order to achieve this within the CTT approach, the first step would be to construct the initial data by choosing a conformally flat metric $\bar{\gamma}_{ij} = \delta_{ij}$ as well as $\bar{A}^{ij}_{TT} = 0$. However, after we fix the gauge assuming the MD condition (2.22), there is no remaining freedom to enforce these conditions for $t > 0$ since $h_{ij} \equiv \bar{\gamma}_{ij} - \delta_{ij}$ and $\bar{A}^{ij}_{TT}$ actually satisfy evolution equations. Then, as a possible way to have a fully constrained system of GR equations where the effect of GW in the cosmological dynamics is neglected, following [32, 33] we make the approximations

$$\bar{\gamma}_{ij} = \delta_{ij}, \quad \bar{A}^{ij}_{TT} = 0 \qquad \forall t \,. \tag{2.24}$$

This approach follows the same spirit as the 'waveless theories of gravity' developed originally by Isenberg [35] and later by Wilson and Mathews [36], and its application is supported by previous works from both theoretical and numerical standpoints. In [37] it has been explicitly shown, by using post-Newtonian expansions, that the conformal flatness approximation and the neglect of the TT term (2.24) are accurate even in highly relativistic regimes (further details on this point are discussed the in Appendix of [37]). However, let us remark that these approximations are mainly used to simplify the programming, and they do not represent a fundamental limitation to GRAMSES. As an example, in [38] the authors discuss a 'passive' method to compute the GW emission within this formulation by solving the hyperbolic evolution equations, but without including its back-reaction onto the dynamics of the system, as well as the so-called fully constrained formulation [FCF, 32, 33] in which the latter is properly included. These approaches to go beyond the simple approximations in (2.24) can be particularly well-suited for cosmological applications and straightforwardly implemented in GRAMSES, but these will be left for a future version.

Due to the conformal flatness assumption intrinsic to this scheme, using that $\partial_t \bar{\gamma}^{ij} = 0$ in (2.21) it can be shown that the momentum constraint (2.23) reduces to [33]

$$(\bar{\Delta}_L \beta)^i = 2\partial_j \left( \alpha \psi^{-6} \bar{A}^{ij}_L \right) . \tag{2.25}$$

Then, under this fully constrained formulation of GR the gravitational sector equations can be conveniently solved following the next sequence of steps:

1. Using the CTT decomposition, we solve the momentum constraint (2.15) as an elliptic equation for the longitudinal part of $\bar{A}^{ij}$,
$$(\bar{\Delta}_L W)_i = 8\pi s_i , \tag{2.26}$$
where $s_i \equiv \psi^6 S_i = \gamma^{1/2} S_i$ is the conformal momentum density. After this, we construct the traceless part of the extrinsic curvature as
$$\bar{A}^{ij}_L = (\bar{L}W)^{ij} \equiv \bar{A}^{ij} , \tag{2.27}$$
where in the last step we have neglected $\bar{A}^{ij}_{TT}$ due to the approximation (2.24).

2. We solve the Hamiltonian constraint (2.11), with (2.19) subtracted, as an elliptic equation for the conformal factor $\psi$
$$\bar{\nabla}^2 \psi = -2\pi \psi^{-1} s_0 - \frac{1}{8} \psi^{-7} \bar{A}_{ij} \bar{A}^{ij} + 2\pi \psi^5 \hat{\rho}_m , \tag{2.28}$$

where $s_0 \equiv \psi^6 \rho_m = \gamma^{1/2} \rho_m$ is the conformal matter density. Here $\bar{\nabla}$ is $\bar{D}$ with $\bar{\gamma}_{ij} = \delta_{ij}$ due to the conformal flatness approximation.

3. We determine the lapse function from the CMC slicing condition (2.17)

$$\bar{\nabla}^2(\alpha\psi) = \alpha \left[ 2\pi\psi^{-1}(s_0 + 2s) + \frac{7}{8}\psi^{-7}\bar{A}_{ij}\bar{A}^{ij} + \psi^5 \left( \frac{5K^2}{12} + 2\pi\rho_\Lambda \right) \right] - \psi^5 \dot{K}, \tag{2.29}$$

   where we have used (2.19)-(2.20) as well as defined $s \equiv \psi^6 S = \sqrt{\gamma} S^i_i$.

4. Finally, we determine the shift vector from the momentum constraint (2.25).

5. Then, the current state of the gravitational field is characterised by the spacetime metric

$$ds^2 = -\alpha^2 dt^2 + \psi^4 \delta_{ij}(\beta^i dt + dx^i)(\beta^j dt + dx^j)\,. \tag{2.30}$$

6. The metric (2.30) is used to solve the equations of motion (EOM) for particles, and evolve the system.

Notice that in this scheme (2.29) plays the role analogous to the Poisson equation in Newtonian gravity as it determines the $g_{00}$ metric component $\alpha \sim 1 + \Phi$. However, (2.29) includes a term that is linearly proportional to $\alpha$ and therefore it formally resembles a finite-range (Yukawa-like) potential, which means that the gravitational force appears 'screened' in the CMC gauge. This seems to indicate that it would translate in a suppression of the matter power spectrum at large scales. However, as we will discuss in the cosmological simulation section below, this 'screening' simply represents the effect by the choice of gauge on the simulated matter or velocity power spectrum.

## 3 The matter sector

In GRAMSES we implement a fully general relativistic $N$-body system for dark matter following the ADM formalism, with which we can describe the matter content in the 3-dimensional hypersurface and its time evolution, rather than dealing directly with 4-dimensional quantities. In GR the equation of motion for collisionless particles is the geodesic equation

$$u^\mu \nabla_\mu u_\nu = 0, \tag{3.1}$$

which for the spatial components reads

$$\frac{du_i}{dt} = -\alpha u^0 \partial_i \alpha + u_j \partial_i \beta^j - \frac{u_j u_k}{2u^0} \partial_i \gamma^{jk}\,, \tag{3.2}$$

where the time-component $u^0$ is determined from the normalisation condition $u^\mu u_\mu = -1$ as

$$u^0 = \alpha^{-1} \sqrt{1 + \gamma^{ij} u_i u_j}\,. \tag{3.3}$$

The relation between $u_j$ and the 3-velocity (coordinate velocity) $v^i \equiv dx^i/dt = u^i/u^0$ is

$$\frac{dx^i}{dt} = \frac{\gamma^{ij} u_j}{u^0} - \beta^i. \tag{3.4}$$

Naturally, the Newtonian limit is recovered with $u_i \ll 1$, $\gamma^{ij} \to \delta^{ij}$, $\alpha \to (1 + \Phi_N)$ and $\beta^i \to 0$, where $\Phi_N$ is the Newtonian gravitational potential, in which case (3.2) reduces to Newton's second law (in a comoving coordinate system) and $dx^i/dt = u^i$. Eq. (3.4) shows the nontrivial relationship between the velocities $u_i$ and $u^i$. To be clear, in the code implementation below we shall only use $u_i$ with a lower index, and similarly we always use $\beta^i$ with an upper index.

After we evolve particles with (3.2) and (3.4) we can calculate the matter source terms appearing in the equations for the gravitational sector (2.26)-(2.29). For this purpose, it is convenient to introduce a set of conformal source terms defined as

$$s_0 = \sqrt{\gamma}\rho\,, \tag{3.5}$$

$$s_i = \sqrt{\gamma}S_i\,, \tag{3.6}$$

$$s_{ij} = \sqrt{\gamma}S_{ij}\,. \tag{3.7}$$

We will show below that these quantities are analogous to the usual 'comoving' ones and correspond to those actually determined numerically in the CIC scheme. For example, the 'density' contrast for $s_0$, defined as $\delta s_0/s_0$, corresponds to the local fluctuation of the particle number count rather than the relativistic energy density. This is more convenient in practice because we naturally would like to follow 'particles' rather than the 'density field' in simulations: a same particle can contribute different energy densities at different places, and the relativistic correction effect can be calculated according to the local metric $\gamma_{ij}$. We will discuss the implication of this on the generation of initial conditions in a forthcoming paper.

## 4 Numerical implementation

Let us now describe the actual implementation of the fully constrained formulation of GR and the matter evolution equations in GRAMSES. For this purpose, we recast the GR equations using the code units detailed next. Notice that these are derived from the GR equations in physical units rather in geometric units, i.e., accounting for all $G$ and $c$ factors.

### 4.1 Code units

### 4.1.1 The gravitational sector

In order to implement the GR equations in GRAMSES we introduce a set of dimensionless quantities that are based on $H_0^{-1}$ for measuring time, the box size $L$ for spatial coordinates, the critical density $\rho_c = 3H_0^2/8\pi G$ and the fractional matter density $\Omega_m \equiv \hat{\rho}_{m,0}/\rho_c$ (today's values satisfying the fiducial FLRW equations (2.19) and (2.20)):

$$\tilde{x} = \frac{x}{L}, \qquad d\tilde{t} = H_0\frac{dt}{a^2}, \qquad \tilde{s}_0 = \frac{s_0}{\Omega_m\rho_c}, \qquad \tilde{s}_i = \frac{s_i}{\Omega_m\rho_c c} \qquad \tilde{s} = \frac{s}{\Omega_m\rho_c c}, \tag{4.1}$$

$$\tilde{c} = \frac{c}{LH_0}, \qquad \tilde{K} = a^2\tilde{c}LK, \qquad \tilde{\bar{A}}_{ij} = a^{-1}\tilde{c}L\bar{A}_{ij}, \qquad \tilde{U} = a\tilde{c}^2L^{-1}U, \qquad \tilde{V}_i = a\tilde{c}^2V_i\,, \tag{4.2}$$

$$\tilde{\beta}^i = a^2\tilde{c}\beta^i, \qquad \tilde{b} = a^2\tilde{c}L^{-1}b, \qquad \tilde{B}^i = a^2\tilde{c}B^i\,. \tag{4.3}$$

Notice that, in order to simplify the equations in code units, we have introduced the supercomoving coordinate time $\tilde{t}$ [51], and for $\tilde{s}_i$ and $\tilde{s}$ we have introduced a $c^{-1}$ factor that's not present in $\tilde{s}_0$. In addition, rather than solving the nonlinear equations for the conformal factor and the lapse function, it is more convenient to reparametrise them by definining new variables $\tilde{\Phi}$ and $\tilde{\Psi}$ as

$$\alpha \equiv 1 + \frac{\tilde{\Phi}}{a^2\tilde{c}^2}\,, \tag{4.4}$$

$$\psi \equiv a^{1/2}\left(1 - \frac{\tilde{\Psi}}{2a^2\tilde{c}^2}\right)\,, \tag{4.5}$$

where $\tilde{c}$ is the speed of light in code units. This way, both $\tilde{\Phi}$ and $\tilde{\Psi}$ are quantities measuring deviations from their reference FLRW values (but no linearisation on $\tilde{\Phi}$ or $\tilde{\Psi}$ is carried out). Using this scheme, we can write the momentum constraint (2.26) as

$$(\tilde{\bar{\Delta}}_L \tilde{W})_i = 3\Omega_m a \tilde{s}_i. \tag{4.6}$$

The Hamiltonian constraint (2.28) can be written as

$$\left(1 - \frac{\tilde{\Psi}}{2a^2\tilde{c}^2}\right) \tilde{\bar{\nabla}}^2 \tilde{\Psi} = \frac{3}{2} a\Omega_m \left[\tilde{s}_0 - \left(1 - \frac{\tilde{\Psi}}{2a^2\tilde{c}^2}\right)^6\right] + \frac{\tilde{\bar{A}}_{ij}\tilde{\bar{A}}^{ij}}{4} \left(1 - \frac{\tilde{\Psi}}{2a^2\tilde{c}^2}\right)^{-6} . \tag{4.7}$$

Next, using the the 2nd Friedmann equation (4.12) and the Hamiltonian constraint (4.7), the CMC condition (2.29) in code units becomes

$$\begin{aligned} \tilde{\bar{\nabla}}^2 \left[\tilde{\Phi}\left(1 - \frac{\tilde{\Psi}}{2a^2c^2}\right)\right] =& \frac{Q}{a^2c^2}\tilde{\Phi} + \frac{3a\Omega_m}{2}\left(1 - \frac{\tilde{\Psi}}{2a^2c^2}\right)^{-1}\left[\tilde{s}_0 - \left(1 - \frac{\tilde{\Psi}}{2a^2c^2}\right)^6 + \tilde{s}_m\right] \\ &+ \tilde{\bar{A}}_{ij}\tilde{\bar{A}}^{ij}\left(1 - \frac{\tilde{\Psi}}{2a^2c^2}\right)^{-7} , \end{aligned} \tag{4.8}$$

where

$$Q = \frac{3}{4}a\Omega_m\left(1 - \frac{\tilde{\Psi}}{2a^2c^2}\right)^{-1}\left[\tilde{s}_0 + 5\left(1 - \frac{\tilde{\Psi}}{2a^2c^2}\right)^6 + 2\tilde{s}_m\right] + \frac{7\tilde{\bar{A}}_{ij}\tilde{\bar{A}}^{ij}}{8}\left(1 - \frac{\tilde{\Psi}}{2a^2c^2}\right)^{-7} . \tag{4.9}$$

Finally, the MD condition (2.25) in code units is

$$(\tilde{\bar{\Delta}}_L \tilde{\beta})^i = 2a^3 \tilde{\partial}_j \left(\alpha\psi^{-6}\tilde{\bar{A}}^{ij}\right) . \tag{4.10}$$

In addition, the Friedmann equations (2.19) and (2.20) in code units are

$$\frac{1}{a^4}\frac{\tilde{K}^2}{12} = \frac{3}{4}\Omega_m\left(a^{-3}\hat{\bar{\rho}}_{m,0} + \frac{\Omega_\Lambda}{\Omega_m}\right) , \tag{4.11}$$

$$\frac{1}{a^4}\frac{\tilde{K}^2}{3} - \frac{1}{a^2}\frac{d(a^{-2}\tilde{K})}{d\tilde{t}} = -\frac{3\Omega_m}{2}\left(a^{-3}\hat{\bar{\rho}}_{m,0} + \frac{\Omega_\Lambda}{\Omega_m} + \hat{\tilde{S}}\right) , \tag{4.12}$$

where $\hat{\bar{\rho}}_{m,0} \equiv \hat{\tilde{S}}_0 = 1$ is the homogeneous (comoving) density field in code units, $\Omega_\Lambda \equiv 8\pi G\rho_\Lambda/3H_0^2$, and $\hat{\tilde{S}} = 3\hat{\tilde{P}}$ (with $\tilde{s} = \psi^6\tilde{S}$).

### 4.1.2 The matter sector

For writing the EOM for particles in code units, we introduce the following dimensionless quantities for the particle's 4-velocity and mass:

$$\tilde{u}^\alpha = \frac{u^\alpha}{LH_0} , \quad \tilde{m} = \frac{m}{\Omega_m\rho_c L^3} . \tag{4.13}$$

Then, the system consisting of Eqs. (3.2)-(3.4) becomes

$$\frac{d\tilde{u}_i}{d\tilde{t}} = -\tilde{W}\tilde{c}a^2\tilde{\partial}_i\alpha + \tilde{u}_j\tilde{\partial}_i\tilde{\beta}^j - \alpha\frac{\tilde{u}_j\tilde{u}_k}{2\tilde{W}}\tilde{c}a^2\tilde{\partial}_i\tilde{\gamma}^{jk}\,, \tag{4.14}$$

$$\tilde{v}^i \equiv \frac{d\tilde{x}^i}{d\tilde{t}} = \frac{\tilde{c}}{\tilde{W}}\alpha a^2\gamma^{ij}\tilde{u}_j - \tilde{\beta}^i\,, \tag{4.15}$$

where

$$\tilde{W}^2 \equiv (\alpha\tilde{u}^0)^2 = \tilde{c}^2 + \gamma^{ij}\tilde{u}_i\tilde{u}_j\,, \tag{4.16}$$

is the Lorentz factor in code units.

Finally, for the numerical implementation of the matter source terms in Eqs. (3.5)-(3.7) we need to specify a prescription to calculate them. For this we consider an ensemble of $N$ identical particles of rest mass $m$ treated in a Cloud-in-cell (CIC) scheme. Then, the contributions to each matter source term in Eqs. (3.5)-(3.7) due to a particle at position $(\tilde{x}_p, \tilde{y}_p, \tilde{z}_p)$ can be calculated [52] as

$$(\tilde{s}_0)_{i+1/2\mp1/2,j+1/2\mp1/2,k+1/2\mp1/2} = \frac{\tilde{f}_x^\pm\tilde{f}_y^\pm\tilde{f}_z^\pm}{\Delta\tilde{V}_{ijk}}\frac{\tilde{m}\tilde{W}}{\tilde{c}}, \tag{4.17}$$

$$(\tilde{s}_l)_{i+1/2\mp1/2,j+1/2\mp1/2,k+1/2\mp1/2} = \frac{\tilde{f}_x^\pm\tilde{f}_y^\pm\tilde{f}_z^\pm}{\Delta\tilde{V}_{ijk}}\frac{\tilde{m}\tilde{u}_l}{\tilde{c}}, \tag{4.18}$$

$$(\tilde{s}_{lm})_{i+1/2\mp1/2,j+1/2\mp1/2,k+1/2\mp1/2} = \frac{\tilde{f}_x^\pm\tilde{f}_y^\pm\tilde{f}_z^\pm}{\Delta\tilde{V}_{ijk}}\frac{\tilde{m}\tilde{u}_l\tilde{u}_m}{\tilde{W}\tilde{c}}, \tag{4.19}$$

where

$$\begin{aligned}\tilde{f}_x^+ &\equiv (\tilde{x}_{i+1} - \tilde{x}_p)/\Delta\tilde{x}_i,\\ \tilde{f}_y^+ &\equiv (\tilde{y}_{i+1} - \tilde{y}_p)/\Delta\tilde{y}_i,\\ \tilde{f}_z^+ &\equiv (\tilde{z}_{i+1} - \tilde{z}_p)/\Delta\tilde{z}_i,\end{aligned} \tag{4.20}$$

represent the relative position of the particle inside the $i$-th cell in the $x$, $y$ and $z$ direction, respectively, with $\tilde{f}_y^- = 1 - \tilde{f}_y^+$, $\tilde{f}_y^- = 1 - \tilde{f}_y^+$, $\tilde{f}_z^- = 1 - \tilde{f}_z^+$, and $\Delta\tilde{V}_{ijk} = \Delta\tilde{x}\Delta\tilde{y}\Delta\tilde{z}$ is the cell volume.

In the remainder of this paper we will only deal with quantities in code units and the tilde will be dropped to avoid cluttered notation.

### 4.2 Code structure

Let us now describe the logic flow of the global solution scheme implemented in GRAMSES. We recall that in this code time evolution is only due to particles, and these are evolved in a leapfrog scheme detailed in Appendix A. At a given timestep $n$, using the positions and velocities $\{x^n, u^{n-1/2}\}$ for particles and the GR fields values $\{\Psi^n, \Phi^n, {\beta^i}^n\}$ the code takes the following main steps:

1. Optional (`gr_newtonian`): Solve Newtonian gravity to get $\Phi_N^{n+1}$.

2. Optional (`gr_newtonian`): Temporarily synchronise velocities with $\Phi_N^{n+1}$: $u^{n-1/2} \longmapsto u_N^n$.

3. Calculate the source terms of the GR equations using the currently-available velocity and GR potential fields.

4. Optional (`gr_newtonian`): Revert the temporary synchronisation done in step 5: $u_N^n \longmapsto u^{n-1/2}$.

5. Solve the ten GR field equations: $\{\Psi^n, \Phi^n, \beta^{i^n}\} \longmapsto \{\Psi^{n+1}, \Phi^{n+1}, \beta^{i^{n+1}}\}$.
6. Synchronise velocities (last 'Kick' from previous timestep: $u^{n-1/2} \longmapsto u^n$).
7. Update velocities (first 'Kick' of the current timestep: $u^n \longmapsto u^{n+1/2}$).
8. Update positions using $u^{n+1/2}$ ('Drift': $x^n \longmapsto x^{n+1}$).
9. Go to step 1 with the replacement $n+1 \longmapsto n$ and repeat the process for the next timestep.

We address these points in detail in the next subsections.

### 4.3 Multigrid solver for the gravitational sector

Let us now discuss the main points of the multigrid [53] implementation of the GR equations for the gravitational sector. For this purpose, it is convenient to first split the equations into the Poisson-like ones and the non-Poisson-like ones.

#### 4.3.1 Poisson-like equations

In the solution scheme for the gravitational sector we have eight linear Poisson-type equations arising from the vector Laplacians (4.6) and (4.10) respectively, i.e.,

$$\nabla^2 V_i = 3\Omega_m a s_i, \tag{4.21}$$

$$\nabla^2 U = -\frac{1}{4}\partial_j V^j, \tag{4.22}$$

$$\nabla^2 B^i = 2\partial_j \left[\left(1+\frac{\Phi}{a^2c^2}\right)\left(1-\frac{\Psi}{2a^2c^2}\right)^{-6}\bar{A}^{ij}\right], \tag{4.23}$$

$$\nabla^2 b = -\frac{1}{4}\partial_j B^j, \tag{4.24}$$

where $W_i \equiv V_i + \partial_i U$ and $\beta^i \equiv B^i + \partial^i b$ have been used to cast these equations in the form of a standard Poisson equation.

In order to solve the above equations numerically, we need to represent them in a discrete form. If we consider a uniform grid with cubic cell size $h$, these equations are formally equivalent to

$$\mathcal{L}^h(\varphi^h) = f^h\,, \tag{4.25}$$

where $\mathcal{L}^h$ is the Laplacian operator and $f^h$ a source term. The former is discretised using the standard second order formula

$$\nabla^2\varphi = \frac{1}{h^2}(\varphi_{i+1,j,k} + \varphi_{i-1,j,k} + \varphi_{i,j+1,k} + \varphi_{i,j-1,k} + \varphi_{i,j,k+1} + \varphi_{i,j,k-1} - 6\varphi_{i,j,k})\,, \tag{4.26}$$

where $\varphi_{l,m,n}$ is the value of the field $\varphi$ in the grid cell with index $(l,m,n)$.

The actual discretisation method for $f^h$ depends on the particular source term under consideration. In our implementation, the source $f^h$ for Eq. (4.21) is calculated using the CIC scheme, while the sources for the rest of these equations correspond to divergences which are calculated using finite differences with a 3-point stencil, e.g.,

$$\partial_l V^l = \frac{1}{2h}(V^x_{i+1,j,k} + V^y_{i,j+1,k} + V^z_{i,j,k+1} - V^x_{i-1,j,k} - V^y_{i,j-1,k} - V^z_{i,j,k-1})\,, \tag{4.27}$$

$$\partial_l \bar{A}'^{lm} = \frac{1}{2h}(\bar{A}'^{xm}_{i+1,j,k} + \bar{A}'^{ym}_{i,j+1,k} + \bar{A}'^{zm}_{i,j,k+1} - \bar{A}'^{xm}_{i-1,j,k} - \bar{A}'^{ym}_{i,j-1,k} - \bar{A}'^{zm}_{i,j,k-1})\,, \tag{4.28}$$

where $\bar{A}'^{lm} \equiv \left(1+\frac{\Phi}{a^2c^2}\right)\left(1-\frac{\Psi}{2a^2c^2}\right)^{-6}\bar{A}^{lm}$. The extrinsic curvature term itself is calculated as

$$\bar{A}_{ij} = \partial_i V_j + \partial_j V_i - \frac{1}{2}\delta_{ij}\partial_k V^k + 2\partial_i\partial_j U \,. \tag{4.29}$$

Notice that for the non-diagonal components of $\bar{A}_{ij}$ we need to calculate cross-derivatives of $U$ that depend on the diagonal neighbours of the central cell, for which we use a second-order-accuracy formula. Then, for a cross-derivative in the $xy$ plane (contributing to $\bar{A}_{xy}$) we use the discrete expression

$$\partial_x\partial_y U = \frac{1}{4h^2}\left(U_{i+1,j+1,k} + U_{i-1,j-1,k} - U_{i-1,j+1,k} - U_{i+1,j-1,k}\right), \tag{4.30}$$

and equivalent ones for cross-derivatives in the $xz$ and $yz$ planes.

As a side point, we note that the left-hand sides of Eqs. (4.21)-(4.24) have the 'cyclic' property, e.g., if one sums up the values of $\nabla^2 U$ from all cells with the same $y, z$ (but different $x$) coordinates, the result is zero, which is guaranteed by the nature of finite difference. The same periodic property is also held by the right-hand sides of Eqs. (4.22)-(4.24) by default, which means that these equations are numerically 'self-consistent'. For Eq. (4.21), however, its right-hand side does not automatically satisfy the 'cyclic' property, which could potentially lead to the situation where the two sides of the equation cannot be numerically identical. To prevent this issue, for Eq. (4.21) we have redefined its source term $f^h$ as $f^h - \langle f^h\rangle$, where $\langle f^h\rangle$ is the mean value of $f^h$ on the whole domain grid (the finest grid with uniform resolution that covers the whole simulation box).

The discrete version of Eq. (4.25) is then solved using a Gauss-Seidel (pseudo-time) relaxation method, which after a given number of iterations converges to a solution $\hat{\varphi}^h$. Then, the residual at the fine level is defined as

$$\epsilon^h \equiv \mathcal{L}^h(\hat{\varphi}^h) - f^h \,. \tag{4.31}$$

In order to improve the accuracy of the solution found using relaxation on the fine grid $h$ (and hence reduce $\epsilon^h$), instead of keeping iterating on the same grid we can accelerate the process by moving to a coarser grid with cell size $H = 2h$, which is then associated with the multigrid level $\ell - 1$ (with $\ell$ representing the finest grid). Since in Eq. (4.25) the operator $\mathcal{L}^h(\varphi^h)$ is linear, the coarsified equation is

$$\mathcal{L}^H(\varphi^H) - \mathcal{L}^H(\mathcal{R}\hat{\varphi}^h) \equiv \mathcal{L}^H(\delta\varphi^H) = -\mathcal{R}\epsilon^h \,, \tag{4.32}$$

where $\mathcal{R}$ is the restriction operator and $\delta\varphi^H \equiv \varphi^H - \mathcal{R}\hat{\varphi}^h$. The coarse-level equation (4.32) is then solved using Gauss-Seidel relaxation and the solution $\widehat{\delta\varphi}^H$ found after a given number of iterations is used to correct the fine solution $\hat{\varphi}^h$ by means of a prolongation step

$$\hat{\varphi}^h \leftarrow \hat{\varphi}^h + \mathcal{P}(\widehat{\delta\varphi}^H) \,, \tag{4.33}$$

where $\mathcal{P}$ is the prolongation operator that maps the information from coarse to fine grids. In practice, we use all coarse levels from $(\ell - 1)$ down to 1 (the level at which the whole simulation box is divided into 8 cells) for our multigrid implementation, and arrange them in a 'V-cycle': instead of correcting the level-$\ell$ solution immediately after solving the equation on level-$(\ell - 1)$, the process of solving coarser-level equations goes all the way down to level 1, and the correction process then goes all the way up to level $\ell$. This has greatly improved the speed at which a solution with acceptable accuracy is achieved.

### 4.3.2 Non-Poisson-like equations

Let us now discuss the implementation of the Hamiltonian constraint and the CMC condition, which correspond to the nonlinear PDEs solved in the code.

#### 4.3.2.1 Hamiltonian constraint

In the multigrid language, the Hamiltonian constraint (4.7) at the fine level can be formally written as

$$\mathcal{L}^h(\Psi^h) = f^h \,, \tag{4.34}$$

where

$$\begin{aligned} \mathcal{L}^h(\Psi^h) &\equiv \left(1 - \frac{\Psi^h}{2a^2c^2}\right)\nabla^2\Psi^h + \frac{3}{2}a\Omega_m\left[\left(1 - \frac{\Psi^h}{2a^2c^2}\right)^6 - 1\right] - \frac{\bar{A}_{ij}\bar{A}^{ij}}{4}\left(1 - \frac{\Psi^h}{2a^2c^2}\right)^{-6}, \\ f^h &\equiv \frac{3}{2}a\Omega_m(s_0 - 1)\,. \end{aligned} \tag{4.35}$$

Notice that by keeping the density term $s_0$ in the source $f^h$ (rather than absorbing it in the definition of $\mathcal{L}^h$) we avoid restricting $s_0$ from fine to coarse level, and we only need to restrict the operator coefficient $\bar{A}_{ij}\bar{A}^{ij} \subset \mathcal{L}^h(\Psi^h)$. However, as we discussed above for the case of Poisson-like equations, since our solution needs to satisfy periodic boundary condition, we need to regularise this equation to ensure that the numerical self-consistency condition $\langle \mathcal{L}^h\left(\Psi^h\right)\rangle = 0$ is satisfied[2]. Then, dividing both sides of Eq. (4.34) by $\left(1 - \frac{\Psi^h}{2a^2c^2}\right)$ and taking the mean on both sides, we identify the regularisation term

$$F^h = \frac{3}{2}a\Omega_m\left(1 - \frac{\Psi^h}{2a^2c^2}\right)^{-1}\left[s_0 - \left(1 - \frac{\Psi^h}{2a^2c^2}\right)^6\right] + \frac{\bar{A}_{ij}\bar{A}^{ij}}{4}\left(1 - \frac{\Psi^h}{2a^2c^2}\right)^{-7}, \tag{4.36}$$

and the regularised version of (4.7) solved in the code reads

$$\tilde{\mathcal{L}}^h(\Psi^h) \equiv \mathcal{L}^h(\Psi^h) + \langle F^h\rangle\left(1 - \frac{\Psi^h}{2a^2c^2}\right) = f^h \,, \tag{4.37}$$

which corresponds to a redefinition of our differential operator at the fine level. Then, the residual at the fine level is defined as

$$\epsilon^h_\Psi \equiv \tilde{\mathcal{L}}^h(\hat{\Psi}^h) - f^h \,. \tag{4.38}$$

Next, at level $\ell - 1$ the coarsified version of this nonlinear equation has the generic form

$$\tilde{\mathcal{L}}^H(\Psi^H) = \tilde{\mathcal{L}}^H(\mathcal{R}\hat{\Psi}^h) - \mathcal{R}\epsilon^h_\Psi \,, \tag{4.39}$$

where $\hat{\Psi}^h$ is the solution obtained at the fine level, $\mathcal{R}$ is the restriction operator. In principle we could also regularise the equation at the coarse level, but in practice this is not needed if the fine level is already regularised.

#### 4.3.2.2 The CMC condition

In order to optimally solve the CMC condition (4.8) in the multigrid scheme we introduce the combination

$$\xi \equiv \Phi\left(1 - \frac{\Psi}{2a^2c^2}\right), \tag{4.40}$$

---

[2] Note that in this case $\langle f^h\rangle$ is guaranteed to be zero by the periodic boundary condition of $s_0$ and the subtraction of 1 in Eq. (4.35).

which allows to avoid the usage of additional arrays for storing the restricted field $\Psi$ while solving for $\Phi$ on coarse levels. Then, in terms of $\xi$ the CMC equation (4.8) at the fine level can be written formally as

$$\mathcal{L}^h(\xi^h) = f^h\,, \tag{4.41}$$

where

$$\begin{aligned} \mathcal{L}^h(\xi^h) &\equiv \nabla^2\xi^h - \left(1-\frac{\Psi}{2a^2c^2}\right)^{-1}\frac{Q}{a^2c^2}\xi^h\,, \\ f^h &\equiv \frac{3a\Omega_m}{2}\left(1-\frac{\Psi}{2a^2c^2}\right)^{-1}\left[s_0-\left(1-\frac{\Psi}{2a^2c^2}\right)^6+s_m\right]+\bar{A}_{ij}\bar{A}^{ij}\left(1-\frac{\Psi}{2a^2c^2}\right)^{-7}, \end{aligned} \tag{4.42}$$

and $Q$ is given by (4.9). After subtracting the mean from *both* sides, the regularised equation becomes

$$\mathcal{L}^h(\xi^h) = f^h - \left\langle f^h\right\rangle - \left\langle\left(1-\frac{\Psi}{2a^2c^2}\right)^{-1}\frac{Q^h}{a^2c^2}\xi^h\right\rangle \equiv \tilde{f}^h. \tag{4.43}$$

This means that for solving this equation at the coarse level it is sufficient to restrict the operator coefficient $\left(1-\frac{\Psi}{2a^2c^2}\right)^{-1}\frac{Q}{a^2c^2} \subset \mathcal{L}^h(\xi^h)$. Further, similar to the Poisson-like equations, the regularisation term in (4.43) is absorbed in the source term, so there is no redefinition of the differential operator but of $f^h$. Then, the residual at the fine level in this case is

$$\epsilon^h_\xi \equiv \mathcal{L}^h(\hat{\xi}^h) - \tilde{f}^h\,. \tag{4.44}$$

On the other hand, at $\ell-1$ the coarsified equation is

$$\mathcal{L}^H(\xi^H) = \mathcal{L}^H(\mathcal{R}\hat{\xi}^h) - \mathcal{R}\epsilon^h_\xi\,, \tag{4.45}$$

where $\hat{\xi}^h$ is the solution obtained at the fine level. As in the case of the Hamiltonian constraint, there is no need to regularise this equation at the coarse level.

### 4.4 Particles evolution

After having reconstructed the spacetime by computing the metric components $(\gamma_{ij},\alpha,\beta^i)$ in a fully nonlinear fashion, we can then solve the EOM for particles. Drawing the analogy with the Newtonian case, the geodesic equation can be rewritten effectively as

$$\frac{du_i}{dt} = F_i\,, \tag{4.46}$$

$$\frac{dx^i}{dt} = \left(1+\frac{\Phi}{a^2c^2}\right)\left(1-\frac{\Psi}{2a^2c^2}\right)^{-4}\frac{c}{W}\delta^{ij}u_j - \beta^i\,, \tag{4.47}$$

$$F_i = -\frac{W}{c}\partial_i\Phi + u_j\partial_i\beta^j - \frac{W^2-c^2}{Wc}\frac{1+\frac{\Phi}{a^2c^2}}{1-\frac{\Psi}{2a^2c^2}}\partial_i\Psi\,, \tag{4.48}$$

where

$$W^2 \equiv (\alpha u^0)^2 = c^2 + a^{-2}\left(1-\frac{\Psi}{2a^2c^2}\right)^{-4}\delta^{ij}u_iu_j\,. \tag{4.49}$$

In the Newtonian limit the 'force term' given by (4.48) reduces to $F_i \to -\partial_i\Phi$, but in the GR case this depends not only on gradients of the various gravitational fields (and on the fields themselves), but also on $u_i$. In practice, this means that we cannot compute all the contributions to (4.48) in the same way as the default RAMSES code (or any standard Newtonian code) does. Therefore, in GRAMSES we divide the Kick step (4.46) into a sequence of 5 substeps, each one updating the particle velocity using one force contribution on the right hand side of (4.48), which is decomposed as $F_i = \sum_j c_j (f_j)_i$ with

$$c_j = -u_j \qquad (f_j)_i = -\partial_i \beta^j\,, \qquad j = 1,2,3 \tag{4.50}$$

$$c_4 = \frac{W^2 - c^2}{Wc} \frac{1 + \frac{\Phi}{a^2c^2}}{1 - \frac{\Psi}{2a^2c^2}} \qquad (f_4)_i = -\partial_i \Psi\,, \tag{4.51}$$

$$c_5 = \frac{W}{c} \qquad (f_5)_i = -\partial_i \Phi\,. \tag{4.52}$$

Notice that in doing this we are using the (partially) updated velocity during each substep. Of these five substeps, (4.52) is the dominant one in most realistic situations as it corresponds to the standard Newtonian force in the Newtonian limit.

As an attempt to preserve the Stormer-Verlet scheme as best as we can, the last Kick in the KDK scheme is done following (4.50) to (4.52), i.e., with the largest contribution to $F_i$ included at last (see Appendix A). In contrast, for the first Kick step (before updating the particles' positions) we use the reverse order, i.e., with the largest contribution included first. Again, this is because that, according to the Stormer-Verlet scheme, during the first Kick the 'force' should be evaluated using $u^{n+1/2}$, which implies an implicit equation for the latter (since this is the very velocity that we want to update to). Hence, as an approximation we use the synchronised velocity $u^n$ and the largest contribution during the first substep of the Kick, which then yields a velocity $u_*^{n+1/2}$ that will be the close to $u^{n+1/2}$, and this is then used in the next substeps to calculate the corrections. Finally, the positions are updated in the Drift step (4.47) in a single calculation once the velocities have been fully updated by the previous prescription.

## 4.5 Calculation of matter sources

A key difference in the calculation of the general relativistic matter source terms in Eqs. (3.5)-(3.7) with respect to the Newtonian case is that the former depend not only on $u_i$ but also on $\Psi$ through the Lorentz factor Eq. (4.49). For calculating these we use the already-known values $\Psi^n$, with which the GR equations are solved to get the updated metric components $\{\Psi^{n+1}, \Phi^{n+1}, \beta^{i\,n+1}\}$. This is equivalent to the numerical implementation in the GEVOLUTION code, where the geometric corrections in the energy-momentum tensor at a given timestep are calculated using the values from the previous timestep [19]. More explicitly, the CIC quantities depend on these as

$$s_0 \propto W(\Psi^n, u^{n+1/2})\,, \tag{4.53}$$

$$s_i \propto u_i^{n+1/2}\,, \tag{4.54}$$

$$s_{ij} \propto \frac{u_i^{n+1/2} u_j^{n+1/2}}{W(\Psi^n, u^{n+1/2})}\,. \tag{4.55}$$

Note that as the second 'Kick' step – which takes particle velocities from $u^{n+1/2}$ to $u^{n+1}$ and therefore 'synchronises' particle velocities – is done *after* we solve the GR equations, at the time when the code calculates the matter source terms for the GR equations what are available are the fully updated positions at timestep $(n+1)$, $x^{n+1}$, and the partially-updated velocities $u^{n+1/2}$ (which are still delayed by half a timestep). This issue is not present in the Newtonian case since the gravitational potential (and hence the force) is *independent* of the particle velocities, and we expect that the use of $u^{n+1/2}$ instead of $u^{n+1}$ in the matter source calculation should be a good approximation given the generally small timesteps for simulations.

Nevertheless, GRAMSES has an option to remedy the fact that we only have $u^{n+1/2}$ to calculate the GR source terms, by using a temporary 'Newtonian' synchronisation from solving the standard Newtonian gravity. With this option switched on, the code uses the Newtonian gravitational potential $\Phi_N$ to temporarily update the velocities $u^{n+1/2} \longmapsto u_N^{n+1}$, which are then used to calculate the source terms as a better approximation than using $u^{n+1/2}$ directly in Eqs. (4.53)-(4.55). Then, after the GR equations are solved, we can *exactly revert* the velocities back to $u^{n+1/2}$, before carrying the Kick step normally (see appendix A).

## 5 Code tests

We have performed several code tests for GRAMSES, particularly aimed to test the implementations of the linear and nonlinear solvers of the ten GR potentials as well as the subroutines that calculate new GR quantities used in both field equations and particle evolution equations. The results shown in this Section correspond to simulations with a box size $L = 256$ Mpc/$h$ and $N_p = 256^3$ particles, and since no cosmological evolution is needed for these tests we set the fiducial scale factor to $a = 1$. The discussion on the cosmological GRAMSES runs is presented in Section 6.

### 5.1 Matter and geometric source terms

While in Newtonian $N$-body simulations the matter density field is the only source term feeding the gravitational potential, in GRAMSES the picture is more intricate: the Poisson-like equations (4.21)-(4.24) feature the momentum density $s_i$, the divergence of GR potentials and also that of the traceless part of the extrinsic curvature, i.e., $\partial_j \bar{A}^{ij}$. Furthermore, for the non-Poisson-like equations, (4.7) and (4.8), we also need to calculate terms such as the contraction $\bar{A}_{ij}\bar{A}^{ij}$, the density $s_0$ and the trace $s = \gamma^{ij}s_{ij}$. Clearly, the calculation of the last two quantities is more complicated than that of $s_i$ since they depend nonlinearly on $u_i$ through the Lorentz factor $W$ as can be seen from (4.17)-(4.19). Since in the CIC scheme particles may contribute to different cells depending on their positions, in order to assess the calculation of these quantities, in the tests we fix the particle positions and velocity values by hand, as well as $\Psi$, so we can compare against analytical expressions for the matter source terms.

Figure 1 shows the results for the CIC calculation of $s_0$ and two $s_i$ components when using a uniform particle distribution, a velocity field $u_i = 0.3c \sin 2\pi x_i$ and $\Psi = c^2 \sin 2\pi x \sin 2\pi y \sin 2\pi z$, where $c$ is the speed of light in code units. We find good agreement since the difference with respect to their analytical counterparts remains below $10^{-5}$, and the structures observed for this in the bottom panels of Figure 1 stem from the shape of the functions on the top panels.

Regarding the geometric source terms, in Figure 2 we show the calculation of $\partial_i \bar{A}^{yi}$ and $\bar{A}_{ij}\bar{A}^{ij}$ which involve the discrete formulae, (4.28), (4.29) and (4.30). In order to compare with analytical expressions for this quantities we use $V_i = U = \sin 2\pi x \sin 2\pi y \sin 2\pi z$ as an input for the relevant code subroutines. The agreement found from Fig 2 is roughly one order of magnitude worse than for the matter source terms in Fig 1 but is still nonetheless stays around $10^{-4}$ for both $\partial_i \bar{A}^{yi}$ and $\bar{A}_{ij}\bar{A}^{ij}$. Naturally, the accuracy in the calculation of these quantities is expected to be different as they depend on how fine is the mesh used to perform the finite differences involved in their calculations, and the agreement shown in Fig. 2 is consistent with the grid used for these tests. Similar to Fig. 1, the structure of the difference observed in the bottom panels of Fig. 2 follows from the shape of the testing functions.

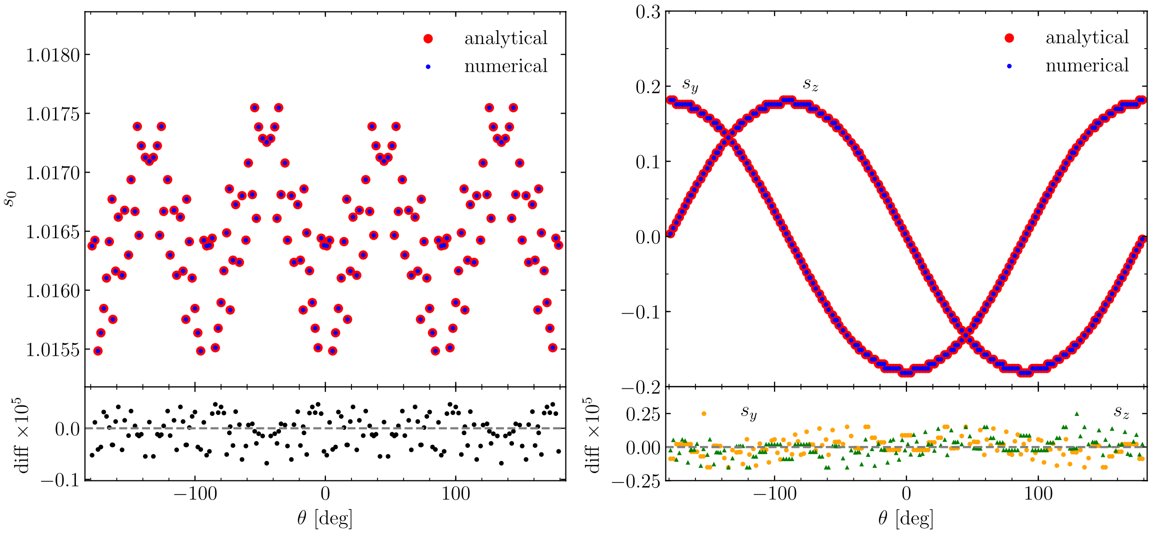

**Figure 1**: GRAMSES calculation of the relativistic matter density $s_0$ (left panel) and momentum density components $s_{y,z}$ (right panel). The values are plotted along a circle with radius $r = \sqrt{x^2 + y^2} = 0.1$ (in code units) measured from the box center in the $y$-$z$ plane, for $\theta \in [-\pi, \pi]$. In the upper panels the blue and red symbols respectively show the code result and the analytical prediction (see the main text for details), while the lower panels show their difference.

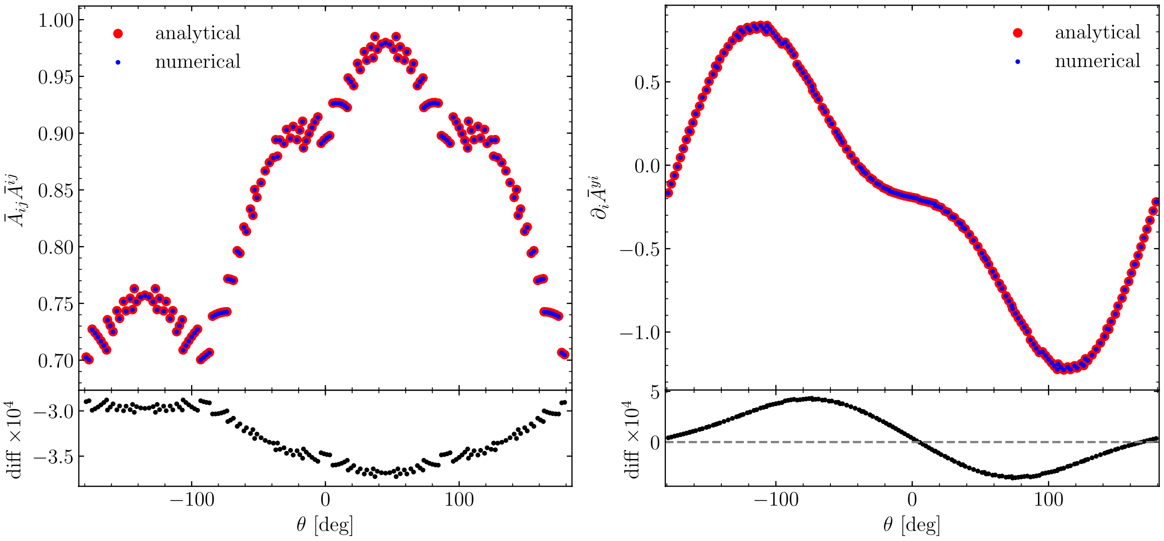

**Figure 2**: The same as Figure 1 but shows the code calculation of the geometric source terms $\bar{A}_{ij}\bar{A}^{ij}$ (left panel) and $\partial_i\bar{A}^{yi}$ (right panel).

We have done similar tests as in Figures 1 and 2, using different choices of particle velocities, and different functional forms for $\Psi$, $U$ and $V_i$. For all these tests we found similar agreement between the code results and the analytical predictions. For simplicity, the extra tests are not shown here.

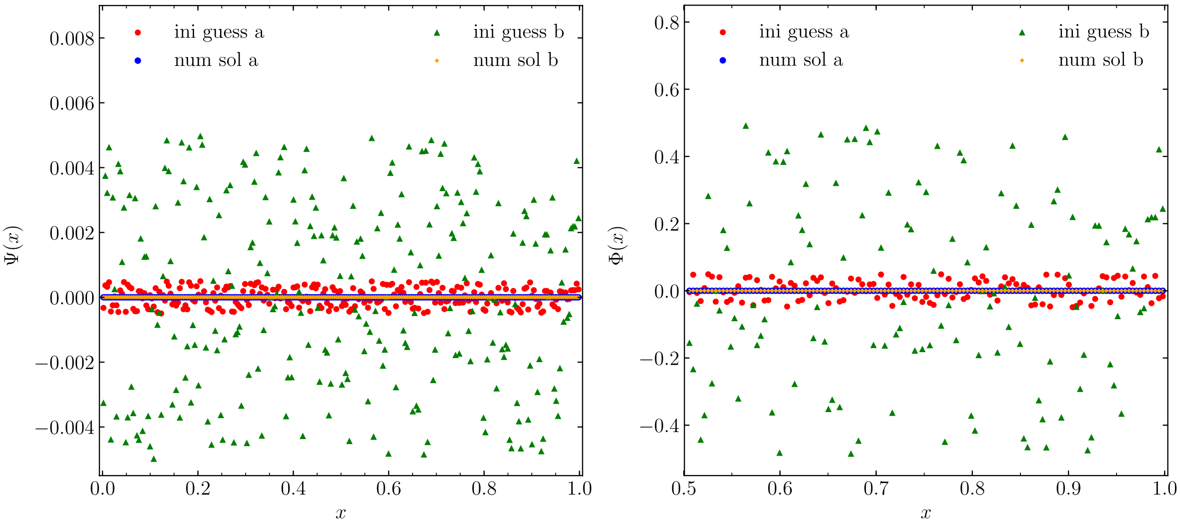

**Figure 3**: Numerical solutions for the GR potentials $\Psi(x)$ (left panel) and $\Phi(x)$ (right panel) obtained through the Gauss-Seidel relaxation method starting from two different sets of initial random guesses (red circles and green triangles) in a FRW (Einstein-de Sitter) universe. The $x$ coordinate spans the whole simulation box in the range $[0, 1]$ in code units. The GRAMSES solutions for both initial guesses (blue circles and orange squares) after relaxation agree well with the analytical solution, which is identically zero (black solid line).

## 5.2 Homogeneous density field

We next show some test cases for the linear and nonlinear equation solvers implemented in GRAMSES. The simplest possibility of such tests for the gravitational sector is to reconstruct the spacetime due to a homogeneous density configuration which corresponds to an FRLW (Einstein-de Sitter) solution. In our test, we set $s_0 = 1$ and $s_i = s = 0$.

Recall that the CMC gauge condition is fixed with the aid of the fiducial Friedmann equations (4.11) and (4.12) and hence the Hamiltonian constraint (4.7) and CMC condition (4.8) have the 'background' solutions $\Psi = \Phi = 0$. Likewise, it is also straightforward to find that the linear GR equations (4.21)-(4.24) are trivially solved, i.e., $V_i = U = B^i = b = 0$, in this case. In Figure 3 we show the numerical solutions for $\Psi$ and $\Phi$ that are obtained by the nonlinear Gauss-Seidel relaxation solver[3] implemented in GRAMSES after performing the relaxation starting from two sets of random initial guesses (green triangles and red circles). As the figure shows, there is a very good agreement in the numerical solutions to both GR potentials regardless of the initial guess from where the relaxation is started.

We have tested the solutions to the other GR potentials, and found similarly good agreements. To save space, here we only show the results for the two most complicated equations.

## 5.3 Point-like, sinusoidal and spherically symmetric sources

In order to add some nontrivial features to the test (as opposed to the case with a homogeneous matter field), we have also tested GRAMSES's relaxation solvers for the Poisson-type and non-Poisson-type equations individually by using various configurations for the source terms. For instance, for the

---

[3] While technically speaking the CMC gauge condition (4.41) is a linear equation, in GRAMSES it is solved using the same nonlinear relaxation solver as in the Halmiltonian constraint (4.34).

Poisson-type equations (4.22)-(4.24) we know that the solution for a point-like source located at $x_p$ is simply given by Green's function

$$\varphi = -\frac{1}{4\pi}\frac{1}{|x - x_p|}\,. \tag{5.1}$$

We test this point-like source scenario by initialising the value of the source in a single cell of the simulation box (at position $x_p$) to a constant: in the case of (4.21) this is equivalent to having a single particle in the center of a cell so that it contributes only to that same cell in the CIC scheme, while for the other linear equations this corresponds to having a non-zero value for their geometric source terms in a single cell of the domain grid.

The left panel of Figure 4 shows the numerical solution to (4.22) in such case and its comparison with the exact analytical solution, (5.1). We note that the numerical solution deviates from the exact one towards the center of the simulation box as well as towards the box boundary. Both discrepancies can be understood in terms of the discrete nature of the numerical simulation: on the one hand, when approaching the source position resolution effects become important and the isotropy respected by the exact solution is broken. On the other hand, towards the box boundary the effect of the finite box size and the periodic boundary conditions imposed on the numerical solution causes deviations from the exact solution (5.1) which decays at infinity. Analogue results for the case of a Schwarzschild spacetime in isotropic coordinates are found in [19] and for point-like mass tests of modified gravity codes, e.g., [54].

The non-Poisson-type equations (4.7) and (4.8) do not have exact analytical solutions for configurations such as point mass to compare against. As an alternative, we have used an inverse approach in which we choose some functional form for $\Psi$ or $\Phi$ by hand and solve (4.7) and (4.8) for some of the source terms under certain simplifications, which can be then used as input to GRAMSES, to check the agreement of its resulting numerical solutions to $\Psi, \Phi$ with the above choices.

In Figure 4 we show the results of such procedure using $\Psi$ with two different functional forms: $\Psi(x) = 10^{-2}\sin 2\pi x$ and $\Psi(r) = \exp\left[-(r-0.5)^2/10^2\right]$ which are then used in Eq. (4.7) to analytically solve for $s_0 = s_0(x)$ and $\bar{A}_{ij}\bar{A}^{ij} = \bar{A}_{ij}\bar{A}^{ij}(r)$, respectively, assuming all other source terms to be zero (here $r$ is measured from the center of the box). These are used as inputs for the GRAMSES nonlinear solver. For the sinusoidal test (middle panel of Figure 4) we find that the numerical solution deviates less than $10^{-5}$ from the exact solution (we also include the initial random guess for the relaxation in that plot), while deviations for the spherically symmetric test (right panel of Figure 4) are larger but still better than those for the point-like test. Similar to the latter case, the numerical solution in the spherically symmetric test also suffers from the effects of periodic boundary conditions which depends on the rate at which the tail of the exponential function decays.

Like before, we have tried more test settings and carried out similar tests for other equations as well. As all the tests result in similar agreement between numerical and exact solutions, we shall not show those tests here to save space.

## 6 Cosmological simulations

In this section we present some of the first results of GRAMSES cosmological simulations in a $\Lambda$CDM universe. For the analyses of the matter and velocity divergence power spectra we use a setup with a box size $L = 4h^{-1}$Gpc and $N_p = 1024^3$ dark matter particles, and we compare against a Newtonian simulation run using the default RAMSES code with identical specifications. In addition, we consider a smaller simulation using $L = 512h^{-1}$Mpc and $N_p = 512^3$, with the AMR option switched off, to generate the different maps shown in Fig. 5 for visualisation. The initial conditions (IC) for both the

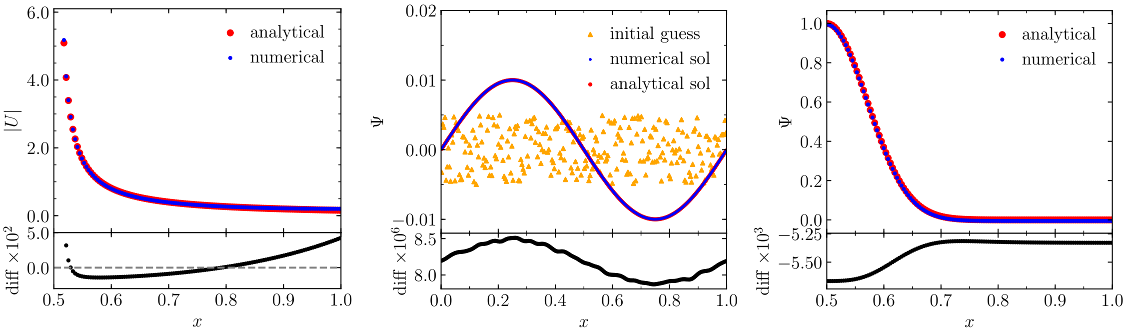

**Figure 4**: Tests of GRAMSES's numerical solutions for the GR potentials obtained through the multigrid Gauss-Seidel relaxation method. *Left panel*: point-like source test for a Poisson-type equation. Here $x$ represents the distance to the point-like source, which is placed in the central cell of the simulation box, in code unit. *Middle panel*: test of the $\Psi$ equation with analytical solution $\Psi = 10^{-2}\sin 2\pi x$ (see the main text for a description of how the test configuration $s_0 = s_0(x)$ is set up). *Right panel*: similar to the middle panel, but for a test configuration for which the $\Psi$ field has a spherically symmetric solution $\Psi(r) = \exp\left[-(r-0.5)^2/10^2\right]$ (using a source $\bar{A}_{ij}\bar{A}^{ij} = \bar{A}_{ij}\bar{A}^{ij}(r)$ as described in the main text); the horizontal coordinate spans half of the simulation box along the $x$ direction, in the range $[0.5, 1]$ in code units. In all cases, the blue and red symbols in the upper subpanel are respectively the numerical and exact analytical solutions, while the lower subpanel shows their difference. The orange symbols in the middle panel are the random initial guess for the relaxation.

GR and the Newtonian simulations are generated using the same random number sequence as seed in order to suppress the effect of realisation scatter in our results. Because GRAMSES works in a different gauge, the generation of IC is nontrivial; here we simply mention that the ICs were generated using a new technique specifically developed for GRAMSES, and will defer a detailed description of that to a forthcoming paper.

Figure 5 is a visual illustration of the maps of three GR matter source terms, $s_0$ (top row), $\theta = \nabla \cdot u$ (middle row) and $s = \gamma^{ij}s_{ij}$ (bottom row), in a slice of constant $z$ coordinate randomly selected from the smaller GRAMSES simulation. The three columns correspond to three different redshifts, $z = 9, 4, 1$ (in the reference cosmology) from left to right. One can see that as time advances and structure formation progresses, finer features start to appear in all three quantities, and their amplitudes also increase. These are as expected. In addition, the main features in all three quantities have good correspondences, with high-density regions having larger values of $s_0, \theta$ and $s$, and vice versa. Note the amplitude of $s$, which has a maximum of order $10^{-4}$ at $z = 1$ that is much smaller than the perturbation in $s_0$; according to Eq. (4.19), this indicates that $(u/c)^2 = (\tilde{u}/\tilde{c})^2 \lesssim \mathcal{O}(10^{-4})$ because in code units $\tilde{m} = 1$.

Figure 6 presents maps from the same slice as Figure 5, but for various GR quantities or their scalar combinations. From top to bottom the rows show respectively $\alpha$, $\psi$, $|\beta|$ (the amplitude of $\beta_i$) and $\bar{A}_{ij}\bar{A}^{ij}$. A logarithmic colour scale is used for $\alpha$, $\psi$ and $\bar{A}_{ij}\bar{A}^{ij}$, while a linear colour scale is used for $|\beta|$, in order to make the features in the maps clearer. To avoid the plot getting too cluttered, we have not shown the colour bars. In all cases, the same colour scheme in Python (the 'jet' scheme) is used, but is 'regulated' such that the reddest (bluest) colour represents the maximum (minimum) of the field values in all pixels of a given map. This is done deliberately: had we used a fixed maximum and minimum value for a quantity at all redshifts, the $z = 9$ maps would appear uniform and almost completely erased of details. In contrast, the 'regulation' not only makes the features at high redshifts clearer, but also demonstrates that, apart from amplitudes, the qualitative patterns of these features barely evolve in time: indeed, there is hardly any visual difference between the left and the middle columns. This is because the GR potentials usually satisfy a Poisson-like equation[4], which in Fourier space takes the form $k^2 \times \text{field} = \text{source}$, so that the field value scales as $k^{-2}$ and so is dominated by the large-scale modes (the reason why the maps in Figure 6 generally lack the much finer details present in the maps of Figure 5). These modes remain linear over time, so that their amplitudes grow quickly while the qualitative patterns change much more slowly. The maps for $\alpha$ and $\psi$ are almost identical, with their colours flipped, which is what is expected from Eqs. (2.28) and (2.29).

Having displayed some visualisation of the simulation outputs from GRAMSES, we next show a few more quantitative results to illustrate that the code works properly.

Figure 7 shows the matter power spectra from the $4h^{-1}$Gpc simulations mentioned above, for six outputting redshifts from $z = 49$ (initial redshift, top left panel) to $z = 1$ (bottom right panel). Within each panel, the top subpanel shows the absolute power spectra and the bottom subpanel shows the relative difference between GRAMSES (CMC-MD-gauge spectrum for the particle number count perturbations, $\delta s_0/s_0$) and RAMSES (synchronous-gauge spectrum for the energy density perturbations, $\delta\rho/\rho$). For comparison, we also show the linear theory predictions for these two spectra using a modified version of the CAMB code [55]: these are respectively the blue and black solid lines in the top subpanels, while the solid lines in the bottom subpanels denote their relative differences. The magenta symbols in the top subpanels show the GRAMSES results as measured using the power spectrum code POWMES [56]: while they agree with linear theory rather well on intermediate and small scales, for the largest scale probed at $z = 49$ POWMES fails to recover the upturn predicted by linear theory (the blue solid line). The orange and red symbols, on the other hand, are the power spectra for the GRAMSES and RAMSES simulations measured using the DTFE code[5] [57], which does capture the upturn. Therefore, in the bottom panels we show the relative differences between the spectra measured using DTFE (red symbols). This comparison poses an interesting question regarding the applicabilities of the different methodologies to calculate the power spectrum when it deviates significantly from the usual behaviour observed in the synchronous gauge[6] (e.g., on large scales due to the gauge difference).

From Figure 7 we see that on large scales the simulation result agrees with linear-theory prediction very well for all redshifts shown. Note that the relative difference between the two power spectra at the largest scale probed by DTFE starts from $\sim 1500\%$ at $z = 49$ and decreases to $\lesssim 20\%$ at $z = 1$, which is a very large range of change that is properly reproduced by GRAMSES. Towards low redshift a small discrepancy from linear theory appears: this is partly because of the smaller differences between the power spectra in the CMC-MD and synchronous gauges, and partly because of the coarse time resolution in our simulation (which has fewer than 50 time steps between $z = 49$ and $z = 1$). Due to the low resolution of the simulation we shall not focus on the results at small scales.

Figure 8 is similar to Fig. 7, but shows the power spectrum of the velocity divergence ($\theta$ defined

---

[4] The deviations from Poisson, such as the inclusion of nonlinear source terms or, like the case of $\bar{\alpha}$, the addition of an extra Yukawa term (i.e., the term linear in $\xi$ in Eq. (4.42)), do not affect the qualitative discussion here.

[5] The DTFE code tessellates the simulation volume following the Delaunay triangulation scheme, where the 3D space is decomposed into tetrahedrons whose vertices are simulation particles. The (density or velocity divergence) field value in each tetrahedron is determined by the corresponding particle quantities (mass and velocity) on its four vertices. The values in the tetrahedrons are then interpolated to a regular grid to give the field values on the latter, from which the corresponding power spectra can be measured using normal fast Fourier transform. This is particularly useful for the velocity field, since it can help to avoid the numerical problem of directly interpolating to a regular grid, which often leads to certain grid cells having zero velocity. See [57] for more details.

[6] Note that at the largest scale probed by POWMES the CMC-MD-gauge power spectrum is nearly two orders of magnitude larger than that in the synchronous gauge.

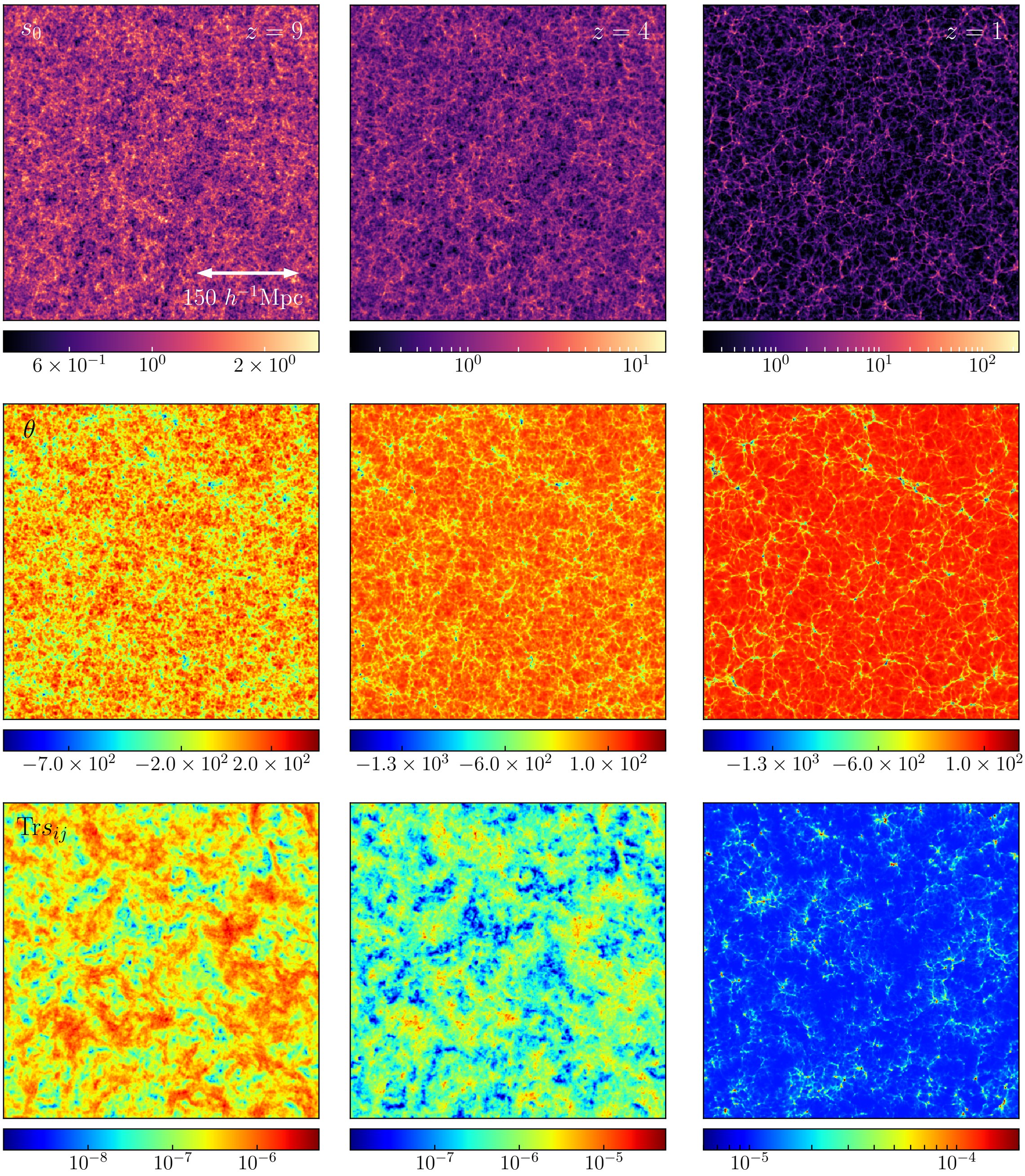

**Figure 5**: The evolution of the three matter sources in GR – the density field $s_0$ (top row), velocity divergence $\theta = \nabla \cdot u$ (middle row) and the trace of the anisotropic stress $s \equiv \mathrm{Tr} s_{ij} = \gamma^{ij} s_{ij}$ (bottom row) – for three redshifts, $z = 49$ (left column), $4$ (middle column) and $1$ (right column). Each panel shows a 2D slice map with constant $z$ coordinate selected from the $512$ Mpc/$h$ GRAMSES simulation box.

above). The blue and black solid lines in the upper subpanels are respectively the velocity convergence power spectra in the CMC and Newtonian gauge calculated by a modified version of the CAMB code, and the solid lines in the lower subpanels are their relative differences. Here all the simulation

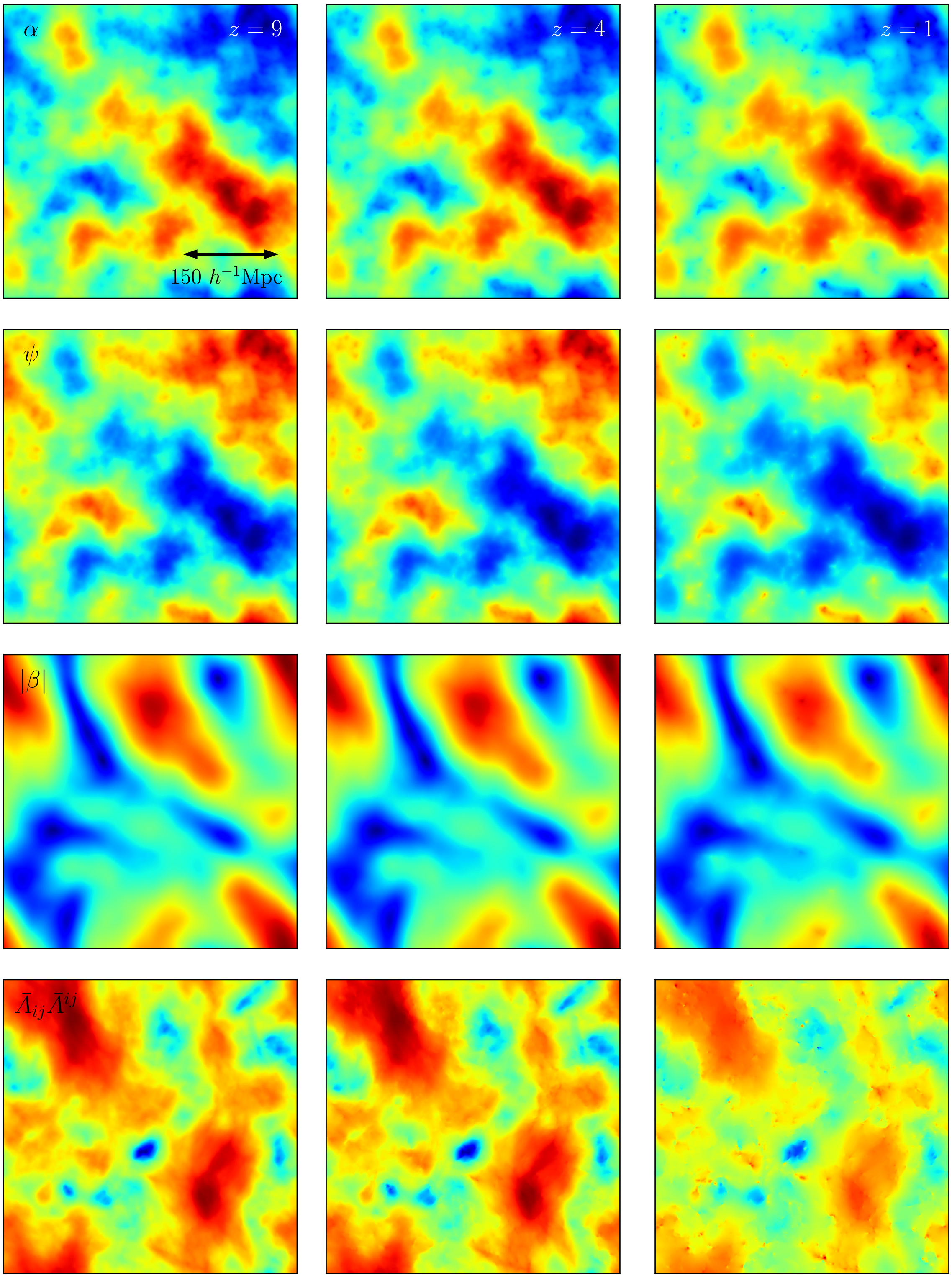

**Figure 6**: As Fig. 5, but for the GR potentials or their scalar combination, $\alpha$ (top row), $\psi$ (second row), $|\beta| \equiv \sqrt{\beta_1^2 + \beta_2^2 + \beta_3^2}$ (third row) and $\bar{A}_{ij}\bar{A}^{ij}$ (bottom row). See the main text for more details.

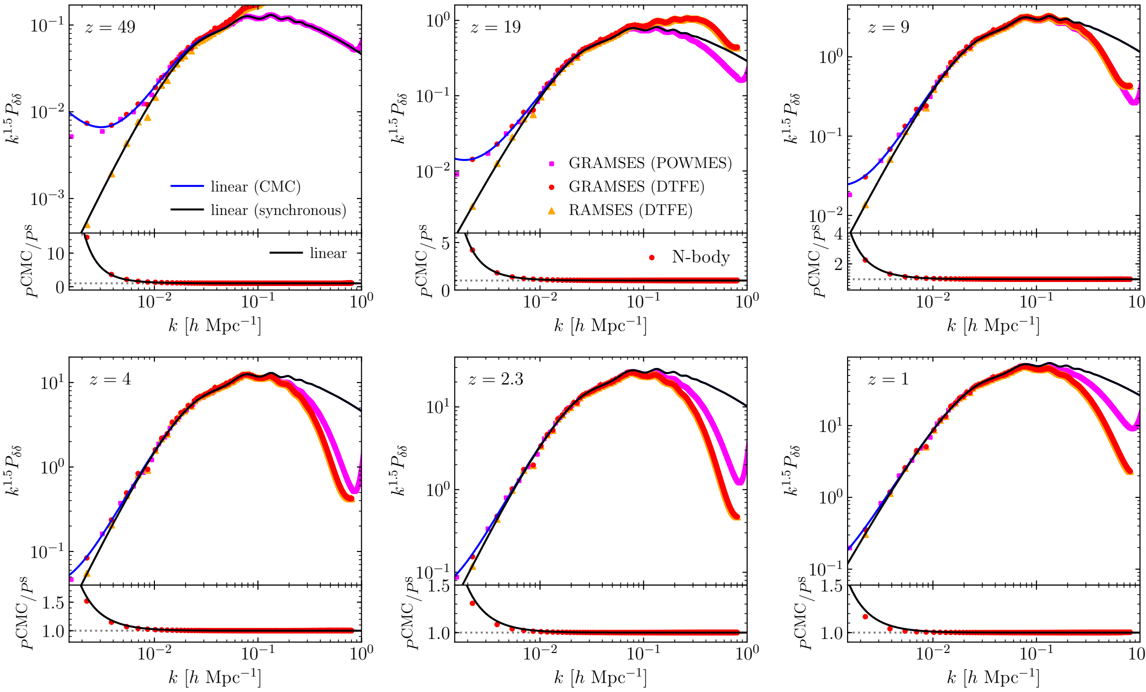

**Figure 7**: The comparison of the matter power spectra from our GRAMSES (GR) and RAMSES (Newtonian) simulations in the $4\ \mathrm{Gpc}/h$ box, at 6 redshifts, from $z = 49$ (upper left) to $z = 1$ (lower right). In each panel, the upper subpanel shows the absolute power spectrum measured using POWMES and DTFE, while the lower subpanel shows the relative difference between GRAMSES and RAMSES. Note that the GRAMSES result is the power spectrum of the particle number count field in the CMC gauge ($P^{\rm CMC}$), while the RAMSES result is that of the energy density field in the synchronous gauge $P^{\rm S}$. The solid lines are the corresponding linear theory predictions for these power spectra obtained using a modified version of CAMB.

spectra have been measured by the DTFE code. A similar level of agreement between the linear theory predictions and simulations to what is shown in Figure 7 can be found here, where at the largest scale probed by DTFE the relative difference between the GRAMSES and RAMSES results changes strongly from $\sim 1000\%$ at $z = 49$ to $\sim 20\%$ at $z = 1$. While the matter power spectra from the GRAMSES GR simulations are consistently higher than those from the RAMSES Newtonian simulations, the velocity power spectra show the opposite trend (this is in agreement with the findings of [58], whose uniform-expansion gauge corresponds to our CMC gauge) – this is partially why the difference between the matter power spectra in the two simulations decreases over time.

Let us remark here that neither the matter power spectrum $P_{\delta\delta}(k)$ nor the velocity divergence power spectrum $P_{\theta\theta}$ are gauge invariant quantities and the differences on large scales seen in Figures 7 and 8 are therefore not physical effects. However, being able to reproduce the expected gauge effects in our simulations is a useful test of the numerical implementation itself. We have stated briefly above that the $P_{\delta\delta}$ measured from the GRAMSES simulations are the power spectra for the particle number count perturbations in the CMC-MD gauge, while the $P_{\delta\delta}$ measured from the RAMSES simulations are for the energy density field in the synchronous gauge. We have also compared $P_{\theta\theta}$ from RAMSES with the Newtonian gauge results from linear theory. These issues are indeed intricately related to the fact that the initial conditions in our GR simulations have to be generated in a way compatible with

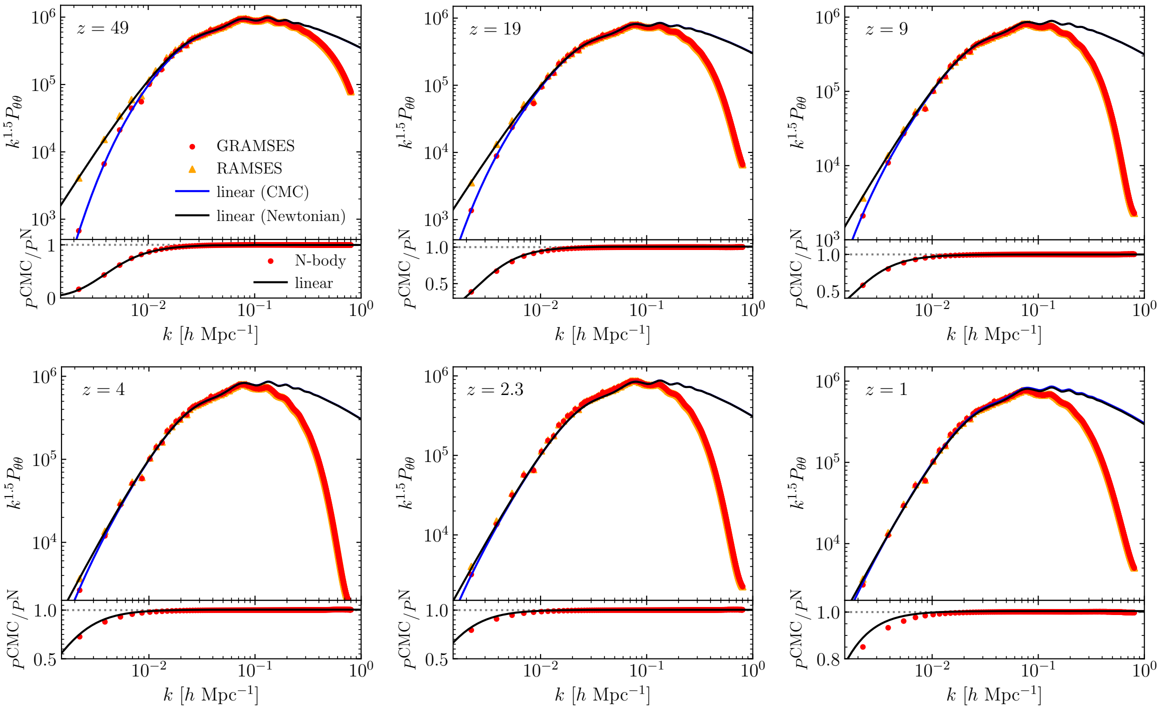

**Figure 8**: The same as Figure 7, but shows the velocity divergence power spectra predicted by the 4 Gpc/$h$ GRAMSES (GR) and RAMSES (Newtonian) simulations. The former makes use of the CMC-MD gauge, while the latter follows the velocity field in the Newtonian gauge. All simulation results are measured using DTFE, and the solid lines are the linear-theory predictions obtained using a modified version of CAMB.

our gauge choice (see, e.g., [59–61]), and as mentioned above these topics will be discussed in depth in a forthcoming paper.

## 7 Discussion and conclusions

In this work we have presented GRAMSES, a new implementation of general relativistic $N$-body AMR simulations in cosmology. This code brings together the advantages of current Numerical Relativity codes, in particular the decomposition of the Einstein equations using the 3+1 ADM formalism, and the $N$-body particle methods for standard cosmological simulations, so that it can accurately solve the nonlinear Einstein equations all the way down to deeply nonlinear scales on which particle orbit crossing is frequent. We have discussed the relevant theoretical background upon which this is based as well as its numerical implementation in detail. The current implementation of GRAMSES does not include the evolution equations of the dynamical degrees of freedom in the gravitational sector, the omission of which is expected to have negligible impact on cosmological simulations. However, we emphasise that this is not a fundamental limitation of our framework, and indeed the implementation of the evolution equations in GRAMSES is currently undergoing.

Multigrid relaxation, adaptive mesh refinement and efficient MPI parallelisation are three of the key features of GRAMSES, which are inherited from its parent code – the publicly-available $N$-body and hydrodynamical simulation solver RAMSES [31]. These are what will enable GRAMSES to run large simulations for cosmological volumes while at the same time resolving scales well within virialised structures. In this paper we have opted to not devote much space to the description of these features, as they are well-established techniques nowadays and a lot of details can be found from the RAMSES code paper, references therein and its derived literature. However, let us briefly mention that the computation of geometric source terms for the Einstein equations in the ADM formalism – such as $\bar{A}_{ij}\bar{A}^{ij}$ and $\partial_i\bar{A}^{ij}$ – are actually nontrivial at the boundaries of refined meshes, which is largely due to the fact that $\bar{A}_{ij}$ itself already involves up to second-order derivatives of the GR potentials $V_i$ and $U$. Furthermore, the use of AMR increases the memory requirement of the code: without AMR, the different GR potentials, for a given time step, can be calculated sequentially so that a same array can be recycled for storing them; with AMR and the associated adaptive timestepping, the GR potentials must be kept for longer because they are needed to set up the boundary conditions for the refinement in all subtimesteps, and so we opt to create a separate array for each GR potential.

We have conducted various code tests to verify that all the source terms are computed correctly and that the multigrid relaxation solvers implemented are giving the correct solutions for test cases where the exact solutions are known or can be derived in alternative ways. We also successfully run a cosmological simulation for a $\Lambda$CDM universe in a general relativistic setting. The maps produced in this GR simulation show expected features, and a more detailed quantitative analysis shows that the matter and velocity power spectra from the GR simulation display the expected behaviour for the CMC-MD gauge on large scales.

The generation of initial condition for GRAMSES simulations will be addressed in a forthcoming paper. Nonetheless, we can mention here that in order to generate initial conditions in the CMC-MD gauge we have modified the CAMB and 2LPTic [62] codes. The former is used to generate the matter power spectrum implementing the gauge transformations at the initial redshift $z_{\rm ini}$ of the simulation, but also on two neighbouring ones (one at a slightly higher while the other a slightly lower redshift). Then, our modified 2LPTic code realizes this power spectrum to calculate the particle positions in the standard way, but the velocity is calculated by finite differencing the particle displacements of the two neighbouring snapshots. This has the advantage of being independent of an explicit parameterisation of the growth factor (and growth rate) which can become scale-dependent in certain gauges and dark energy/modified gravity models and thus violate a basic assumption (scale-independent linear growth rate) of the default 2LPTic code.

The code can be particularly useful for capturing relativistic effects in large-scale simulations as well as for studying problems beyond the Newtonian approximation such as the effect of large density contrasts on the surrounding spacetime and its impact on the estimation of cosmological parameters. Due to perturbed photon geodesics, distant objects can have observed redshifts, angular positions and fluxes which deviate from the true values. This can lead to various effects in observations such as in the galaxy density field [63–65]. While subtle, these effects are detectable using suitable estimators, and their detectability varies with redshift, scale and estimator [e.g., 66–72]. To fully accurately study such effects in future galaxy surveys and how they could impact on the estimation of cosmological parameters and constraints on models, realistic mock galaxy catalogues based on cosmological simulations are needed [69]; such simulations should ideally have large volumes to capture the very large scale effects, but also resolve nonlinear scales and even virialised objects to more accurately predict the nonlinear effects [e.g., 73, 74]. Another interesting topic is the back-reaction effect of space-time averaging on the expansion rate [4], an effect the exact size of which is still being debated and which can have important implications on the understanding of the cosmic acceleration or cosmological parameter estimations, which is a nonlinear effect that cannot be fully captured by linear perturbation theory [13] and is therefore better to be quantified using $N$-body simulations that solve the nonlinear Einstein equations inside the most nonlinear virialised objects.

As mentioned above, GRAMSES can be extended to implement the GR evolution equations in the FCF formulation, which will allow for the addition of gravitational wave propagation, for specific astrophysics models of the GW source distribution, into large cosmological simulations. In addition, the implementation of scalar field dark energy or modified gravity models in GRAMSES is potentially interesting as it would allow to study the evolution of the new degrees of freedom inside virialised dark matter haloes and their impact on the GR effects [75, 76].

## Acknowledgments

We are grateful to Marius Cautun for the help with the DTFE code, and to Marco Bruni and Kazuya Koyama for useful discussions and comments on this work. CB-H is supported by the Chilean National Commission for Scientific and Technological Research through grant CONICYT/Becas-Chile (No. 72180214). BL is supported by STFC Consolidated Grant (Nos. ST/I00162X/1, ST/P000541/1) and a European Research Council Starting Grant (ERC-StG-716532-PUNCA). This work used the DiRAC@Durham facility managed by the Institute for Computational Cosmology on behalf of the STFC DiRAC HPC Facility (`www.dirac.ac.uk`). The equipment was funded by BEIS via STFC capital grants ST/K00042X/1, ST/P002293/1, ST/R002371/1 and ST/S002502/1, Durham University and STFC operation grant ST/R000832/1. DiRAC is part of the UK National e-Infrastructure.

## A Leapfrog scheme for time evolution of particles

GRAMSES uses the usual leapfrog or Stormer-Verlet scheme for particle movements. In this scheme, the position and momentum (or velocity) of a given particle from step $n$ to step $(n+1)$, with a time interval $\Delta t$, are updated using the following prescription,

$$p^{n+1/2} = p^n - \frac{\Delta t}{2} H_x\left(x^n, p^{n+1/2}\right), \tag{A.1}$$

$$x^{n+1} = x^n + \frac{\Delta t}{2}\left[H_p(x^n, p^{n+1/2}) + H_p(x^{n+1}, p^{n+1/2})\right], \tag{A.2}$$

$$p^{n+1} = p^{n+1/2} - \frac{\Delta t}{2} H_x\left(x^{n+1}, p^{n+1/2}\right), \tag{A.3}$$

where $n+1/2$ is the middle between the two neighbouring timesteps $t^n$ and $t^{n+1}$, $p$ is the conjugated momenta to the canonical variable $x$, $H(x,p)$ is the Hamiltonian of the system, and $H_x, H_p$ are the partial derivatives of $H(x,p)$ with respect to $x$ and $p$ respectively. In the case of Newtonian gravity $H = p^2/2m + \Phi_N(x)$, where $p = mv$ and $\Phi_N(x)$ is the Newtonian gravitational potential, the Hamiltonian $H$ is completely separable for $x$ and $v$, and the above operations reduce to the standard Kick-Drift-Kick (KDK) scheme

$$v^{n+1/2} = v^n - \frac{\Delta t}{2}\partial_x \Phi_N(x^n) \tag{A.4}$$

$$x^{n+1} = x^n + \Delta t \cdot v^{n+1/2} \tag{A.5}$$

$$v^{n+1} = v^{n+1/2} - \frac{\Delta t}{2}\partial_x \Phi_N(x^{n+1}) \tag{A.6}$$

Apparently, this makes the system explicit, i.e., the right-hand sides of Eqs. (A.4)-(A.6) do not depend on the quantities (which are at step $(n+1)$) on the left-hand sides. Although from Eqs. (A.4) and (A.6) it would seem that we need to do two force calculations per time step, this is not actually the case since $\partial_x\Phi_N(x^{n+1})$ in (A.6) is the same as the force in (A.4) in the next step, so the second Kick (A.6) operation can wait until the following (i.e., the $(n+1)$th) timestep when $\Phi_N(x^{n+1})$ has been solved. In other words, in practice the second Kick operation (A.6) for the $n$the timestep is done after the Newtonian potential is solved in the $(n+1)$th timestep; in RAMSES this is called synchronisation as it finally 'synchronises' all particle velocities to the correct time before these velocities can be used to move (Drift) the particles.

In the case of GR, the Hamiltonian of a free particle,in the 3+1 formalism is

$$H = \alpha\sqrt{m^2 + \gamma^{ij} p_i p_j} - \beta^i p_i \tag{A.7}$$

where $p_i = m u_i$ is the (spatial) momentum. Using Hamilton's equations

$$\frac{dx^i}{dt} = \frac{\partial H}{\partial p_i}\,, \tag{A.8}$$

$$\frac{dp_i}{dt} = -\frac{\partial H}{\partial x^i}\,, \tag{A.9}$$

we can derive the equation of motion for this system, i.e., the geodesic equations (4.46)-(4.48). We note that in this case the Hamiltonian (A.7) is not separable, because there is the multiplication of $\gamma^{ij}$ (which depends on $x$) and $p_i p_j$ under the square root. Therefore, the leapfrog system (A.1)-(A.3) is implicit and not straightforward to implement as in the Newtonian case. The simplest approximation to make the system explicit is to evaluate the Hamiltonian derivatives at the wrong phases, i.e.,

$$u^{n+1/2} = u^n + \frac{\Delta t}{2} F(x^n, u^n), \tag{A.10}$$

$$x^{n+1} = x^n + \Delta t \mathcal{V}(x^n, u^{n+1/2}), \tag{A.11}$$

$$u^{n+1} = u^{n+1/2} + \frac{\Delta t}{2} F(x^{n+1}, u^{n+1/2}), \tag{A.12}$$

where

$$F_i = -\frac{W}{c}\partial_i\Phi + u_j\partial_i\beta^j - \frac{W^2 - c^2}{Wc}\frac{1+\frac{\Phi}{a^2c^2}}{1-\frac{\Psi}{2a^2c^2}}\partial_i\Psi\,, \tag{A.13}$$

$$\mathcal{V}^i = \left(1+\frac{\Phi}{a^2c^2}\right)\left(1-\frac{\Psi}{2a^2c^2}\right)^{-4}\frac{c}{W}\delta^{ij}u_j - \beta^i. \tag{A.14}$$

Notice that here, for evaluating $\mathcal{V}(x^n, u^{n+1/2})$ used in (A.11) according to (A.14), we use the current value of the gravitational fields ($\Phi, \Psi, \alpha$ and $\beta_i$) and only the quantities depending on $u_j$ (including $W$) are updated (to $t^{n+1/2}$). Likewise, in (A.12) the force term $F(x^{n+1}, u^{n+1/2})$ uses the updated velocities for the explicit dependence on $u^{n+1/2}$ as well as for the source terms for the fields at the new timestep. Finally, for repeating the process, in (A.10) we use the updated velocities for the explicit dependences on $u^n$ and geometric fields based on the updated particles positions (with sources at $u^{n+1/2}$).

Let us remark that even if in the Hamiltonian formalism the variables $(x, p)$ are independent (conjugated) variables, and in the second Kick step (A.12) the various gravitational fields appearing in $F(x^{n+1}, u^{n+1/2})$ are solved at the final positions, e.g. $\Phi(x^{n+1})$, the source terms for their equations have used the velocities $u^{n+1/2}$ because we have not yet synchronised by the time we evaluate these sources at timesteim $(n+1)$, and thus the fields carry a delayed information about the velocities by half a timestep. Again, this issue is not present in the Newtonian case since the gravitational field $\Phi_N$ is only sourced by the mass density field which depends only on the particles position but not on their velocities. A possible way to get around this is to temporarily update the velocity before carrying

(A.12) using Poisson equation for the Newtonian gravitational potential $\Phi_N$, giving us an estimated updated velocity, namely

$$u_N^{n+1} = u^{n+1/2} - \frac{\Delta t}{2} \partial_x \Phi_N \,, \tag{A.15}$$

which can be used (as an approximation) in the source terms for the GR potentials. After solving the field equations for these the velocity is then reverted back to $u^{n+1/2}$, after which 'true' synchronisation (A.12) is performed.

In principle, the above scheme could be further improved by introducing an extra step to update the position in such a way that the symplecticity of the scheme is restored (although time-reversal invariance is still broken). However, since for simulations with AMR the adaptive timesteps render the KDK scheme non-symplectic even in the Newtonian case, we shall not explain these alternatives, which are more complicated, in detail here.

## References

[1] D. H. Weinberg, M. J. Mortonson, D. J. Eisenstein, C. Hirata, A. G. Riess and E. Rozo, *Observational Probes of Cosmic Acceleration*, *Phys. Rept.* **530** (2013) 87 [`1201.2434`].

[2] R. Laureijs, J. Amiaux, S. Arduini, J. L. Augueres, J. Brinchmann, R. Cole et al., *Euclid Definition Study Report*, *ArXiv e-prints* (2011) [`1110.3193`].

[3] DESI collaboration, A. Aghamousa et al., *The DESI Experiment Part I: Science,Targeting, and Survey Design*, `1611.00036`.

[4] T. Buchert and S. Räsänen, *Backreaction in late-time cosmology*, *Ann. Rev. Nucl. Part. Sci.* **62** (2012) 57 [`1112.5335`].

[5] V. Springel et al., *Simulating the joint evolution of quasars, galaxies and their large-scale distribution*, *Nature* **435** (2005) 629 [`astro-ph/0504097`].

[6] M. Vogelsberger, S. Genel, V. Springel, P. Torrey, D. Sijacki, D. Xu et al., *Properties of galaxies reproduced by a hydrodynamic simulation*, *Nature* **509** (2014) 177 [`1405.1418`].

[7] J. Schaye et al., *The EAGLE project: Simulating the evolution and assembly of galaxies and their environments*, *Mon. Not. Roy. Astron. Soc.* **446** (2015) 521 [`1407.7040`].

[8] T. Buchert and J. Ehlers, *Averaging inhomogeneous Newtonian cosmologies*, *Astron. Astrophys.* **320** (1997) 1 [`astro-ph/9510056`].

[9] N. Kaiser, *Why there is no Newtonian backreaction*, *Mon. Not. Roy. Astron. Soc.* **469** (2017) 744 [`1703.08809`].

[10] T. Buchert, *On Backreaction in Newtonian cosmology*, *Mon. Not. Roy. Astron. Soc.* **473** (2018) L46 [`1704.00703`].

[11] A. G. Riess et al., *A 2.4% Determination of the Local Value of the Hubble Constant*, *Astrophys. J.* **826** (2016) 56 [`1604.01424`].

[12] PLANCK collaboration, N. Aghanim et al., *Planck 2018 results. VI. Cosmological parameters*, `1807.06209`.

[13] E. Bentivegna and M. Bruni, *Effects of nonlinear inhomogeneity on the cosmic expansion with numerical relativity*, *Phys. Rev. Lett.* **116** (2016) 251302 [`1511.05124`].

[14] H. Macpherson, D. J. Price and P. D. Lasky, *Einstein's Universe: Cosmological structure formation in numerical relativity*, `1807.01711`.

[15] J. Adamek, D. Daverio, R. Durrer and M. Kunz, *General Relativistic $N$-body simulations in the weak field limit*, *Phys. Rev.* **D88** (2013) 103527 [`1308.6524`].

[16] J. Adamek, R. Durrer and M. Kunz, *N-body methods for relativistic cosmology*, *Class. Quant. Grav.* **31** (2014) 234006 [`1408.3352`].

[17] J. Adamek, C. Clarkson, R. Durrer and M. Kunz, *Does small scale structure significantly affect cosmological dynamics?*, *Phys. Rev. Lett.* **114** (2015) 051302 [`1408.2741`].

[18] J. Adamek, D. Daverio, R. Durrer and M. Kunz, *General relativity and cosmic structure formation*, *Nature Phys.* **12** (2016) 346 [`1509.01699`].

[19] J. Adamek, D. Daverio, R. Durrer and M. Kunz, *gevolution: a cosmological N-body code based on General Relativity*, *JCAP* **1607** (2016) 053 [`1604.06065`].

[20] J. Adamek, R. Durrer and M. Kunz, *Relativistic N-body simulations with massive neutrinos*, *JCAP* **1711** (2017) 004 [`1707.06938`].

[21] D. S. Goldwirth and T. Piran, *Spherical inhomogeneous cosmologies and inflation: Numerical methods*, *Phys. Rev.* **D40** (1989) 3263.

[22] J. B. Mertens, J. T. Giblin and G. D. Starkman, *Integration of inhomogeneous cosmological spacetimes in the BSSN formalism*, *Phys. Rev.* **D93** (2016) 124059 [`1511.01106`].

[23] H. J. Macpherson, P. D. Lasky and D. J. Price, *Inhomogeneous Cosmology with Numerical Relativity*, *Phys. Rev.* **D95** (2017) 064028 [`1611.05447`].

[24] F. Löffler, J. Faber, E. Bentivegna, T. Bode, P. Diener, R. Haas et al., *The einstein toolkit: a community computational infrastructure for relativistic astrophysics*, *Classical and Quantum Gravity* **29** (2012) 115001.

[25] T. Nakamura, K. Oohara and Y. Kojima, *General relativistic collapse to black holes and gravitational waves from black holes*, *Progress of Theoretical Physics Supplement* **90** (1987) 1.

[26] M. Shibata and T. Nakamura, *Evolution of three-dimensional gravitational waves: Harmonic slicing case*, *Phys. Rev. D* **52** (1995) 5428.

[27] T. W. Baumgarte and S. L. Shapiro, *On the numerical integration of Einstein's field equations*, *Phys. Rev.* **D59** (1999) 024007 [`gr-qc/9810065`].

[28] W. E. East, R. Wojtak and T. Abel, *Comparing Fully General Relativistic and Newtonian Calculations of Structure Formation*, *Phys. Rev.* **D97** (2018) 043509 [`1711.06681`].

[29] D. Daverio, Y. Dirian and E. Mitsou, *General Relativistic Cosmological N-body Simulations I: time integration*, `1904.07841`.

[30] R. Arnowitt, S. Deser and C. W. Misner, *Dynamical structure and definition of energy in general relativity*, *Phys. Rev.* **116** (1959) 1322.

[31] R. Teyssier, *Cosmological hydrodynamics with adaptive mesh refinement: a new high resolution code called ramses*, *Astron. Astrophys.* **385** (2002) 337 [`astro-ph/0111367`].

[32] S. Bonazzola, E. Gourgoulhon, P. Grandclément and J. Novak, *Constrained scheme for the einstein equations based on the dirac gauge and spherical coordinates*, *Phys. Rev. D* **70** (2004) 104007.

[33] I. Cordero-Carrion, J. M. Ibanez, E. Gourgoulhon, J. L. Jaramillo and J. Novak, *Mathematical Issues in a Fully-Constrained Formulation of Einstein Equations*, *Phys. Rev.* **D77** (2008) 084007 [`0802.3018`].

[34] L. E. Kidder, M. A. Scheel and S. A. Teukolsky, *Extending the lifetime of 3-D black hole computations with a new hyperbolic system of evolution equations*, *Phys. Rev.* **D64** (2001) 064017 [`gr-qc/0105031`].

[35] J. A. Isenberg, *Waveless approximation theories of gravity*, *Int. J. Mod. Phys.* **D17** (2008) 265 [`gr-qc/0702113`].

[36] J. R. Wilson and G. J. Mathews, *Relativistic hydrodynamics.*, pp. 306–314. 1989.

[37] I. Cordero-Carrión, P. Cerdá-Durán, H. Dimmelmeier, J. L. Jaramillo, J. Novak and E. Gourgoulhon, *Improved constrained scheme for the einstein equations: An approach to the uniqueness issue*, *Phys. Rev. D* **79** (2009) 024017.

[38] I. Cordero-Carrion, P. Cerda-Duran and J. M. Ibanez, *Gravitational waves in dynamical spacetimes with matter content in the Fully Constrained Formulation*, *Phys. Rev.* **D85** (2012) 044023 [`1108.0571`].

[39] M. Alcubierre, *Introduction to 3+1 numerical relativity*, International series of monographs on physics. Oxford Univ. Press, Oxford, 2008.

[40] T. W. Baumgarte and S. L. Shapiro, *Numerical relativity: solving Einstein's equations on the computer*. Cambridge University Press, 2010.

[41] S. Masaru, *Numerical Relativity*, 100 Years Of General Relativity. World Scientific Publishing Company, 2015.

[42] A. Lichnérowicz, *Sur les équations relativistes de la gravitation*, *Bulletin de la Société Mathématique de France* **80** (1952) 237.

[43] J. W. York, Jr., *Kinematics and dynamics of general relativity*, in *Sources of Gravitational Radiation* (L. L. Smarr, ed.), pp. 83–126, 1979.

[44] L. Smarr and J. W. York, *Kinematical conditions in the construction of spacetime*, *Phys. Rev. D* **17** (1978) 2529.

[45] J. T. Giblin, J. B. Mertens and G. D. Starkman, *A cosmologically motivated reference formulation of numerical relativity*, *Class. Quant. Grav.* **34** (2017) 214001 [`1704.04307`].

[46] J. T. Giblin, J. B. Mertens, G. D. Starkman and C. Tian, *The Limited Accuracy of Linearized Gravity*, `1810.05203`.

[47] L. Smarr and J. W. York, *Radiation gauge in general relativity*, *Phys. Rev. D* **17** (1978) 1945.

[48] LIGO Scientific Collaboration and Virgo Collaboration collaboration, B. P. Abbott, R. Abbott, T. D. Abbott, M. R. Abernathy, F. Acernese, K. Ackley et al., *Observation of gravitational waves from a binary black hole merger*, *Phys. Rev. Lett.* **116** (2016) 061102.

[49] LIGO Scientific, Virgo, Fermi GBM, INTEGRAL, IceCube, AstroSat Cadmium Zinc Telluride Imager Team, IPN, Insight-Hxmt, ANTARES, Swift, AGILE Team, 1M2H Team, Dark Energy Camera GW-EM, DES, DLT40, GRAWITA, Fermi-LAT, ATCA, ASKAP, Las Cumbres Observatory Group, OzGrav, DWF (Deeper Wider Faster Program), AST3, CAASTRO, VINROUGE, MASTER, J-GEM, GROWTH, JAGWAR, CaltechNRAO, TTU-NRAO, NuSTAR, Pan-STARRS, MAXI Team, TZAC Consortium, KU, Nordic Optical Telescope, ePESSTO, GROND, Texas Tech University, SALT Group, TOROS, BOOTES, MWA, CALET, IKI-GW Follow-up, H.E.S.S., LOFAR, LWA, HAWC, Pierre Auger, ALMA, Euro VLBI Team, Pi of Sky, Chandra Team at McGill University, DFN, ATLAS Telescopes, High Time Resolution Universe Survey, RIMAS, RATIR, SKA South Africa/MeerKAT collaboration, B. P. Abbott et al., *Multi-messenger Observations of a Binary Neutron Star Merger*, *Astrophys. J.* **848** (2017) L12 [`1710.05833`].

[50] A. Einstein, *Approximative Integration of the Field Equations of Gravitation*, *Sitzungsber. Preuss. Akad. Wiss. Berlin (Math. Phys.)* **1916** (1916) 688.

[51] H. Martel and P. R. Shapiro, *A convenient set of comoving cosmological variables and their application*, *Mon. Not. Roy. Astron. Soc.* **297** (1998) 467 [`astro-ph/9710119`].

[52] M. Shibata, *3-D numerical simulation of black hole formation using collisionless particles: Triplane symmetric case*, *Prog. Theor. Phys.* **101** (1999) 251.

[53] W. H. Press, S. A. Teukolsky, W. T. Vetterling and B. P. Flannery, *Numerical Recipes: The Art of Scientific Computing*. Cambridge University Press, 3 ed., 2007.

[54] B. Li, G.-B. Zhao, R. Teyssier and K. Koyama, *ECOSMOG: An Efficient Code for Simulating Modified Gravity*, *JCAP* **1201** (2012) 051 [`1110.1379`].

[55] A. Lewis, A. Challinor and A. Lasenby, *Efficient computation of CMB anisotropies in closed FRW models*, *Astrophys. J.* **538** (2000) 473 [`astro-ph/9911177`].

[56] S. Colombi, A. H. Jaffe, D. Novikov and C. Pichon, *Accurate estimators of power spectra in N-body simulations*, *Mon. Not. Roy. Astron. Soc.* **393** (2009) 511 [`0811.0313`].

[57] M. C. Cautun and R. van de Weygaert, *The DTFE public software - The Delaunay Tessellation Field Estimator code*, `1105.0370`.

[58] S. F. Flender and D. J. Schwarz, *Newtonian versus relativistic cosmology*, *Phys. Rev.* **D86** (2012) 063527 [`1207.2035`].

[59] C. Fidler, T. Tram, C. Rampf, R. Crittenden, K. Koyama and D. Wands, *Relativistic initial conditions for N-body simulations*, *JCAP* **1706** (2017) 043 [`1702.03221`].

[60] C. Fidler, C. Rampf, T. Tram, R. Crittenden, K. Koyama and D. Wands, *General relativistic corrections to $N$-body simulations and the Zel'dovich approximation*, *Phys. Rev.* **D92** (2015) 123517 [`1505.04756`].

[61] W. Valkenburg and B. Hu, *Initial conditions for cosmological N-body simulations of the scalar sector of theories of Newtonian, Relativistic and Modified Gravity*, *JCAP* **1509** (2015) 054 [`1505.05865`].

[62] M. Crocce, S. Pueblas and R. Scoccimarro, *Transients from Initial Conditions in Cosmological Simulations*, *Mon. Not. Roy. Astron. Soc.* **373** (2006) 369 [`astro-ph/0606505`].

[63] J. Yoo, A. L. Fitzpatrick and M. Zaldarriaga, *New perspective on galaxy clustering as a cosmological probe: General relativistic effects*, *Phys. Rev.* **D80** (2009) 083514 [`0907.0707`].

[64] A. Challinor and A. Lewis, *The linear power spectrum of observed source number counts*, *Phys. Rev.* **D84** (2011) 043516 [`1105.5292`].

[65] C. Bonvin and R. Durrer, *What galaxy surveys really measure*, *Phys. Rev.* **D84** (2011) 063505 [`1105.5280`].

[66] C. Bonvin, L. Hui and E. Gaztanaga, *Optimising the measurement of relativistic distortions in large-scale structure*, *JCAP* **1608** (2016) 021 [`1512.03566`].

[67] E. Gaztanaga, C. Bonvin and L. Hui, *Measurement of the dipole in the cross-correlation function of galaxies*, *JCAP* **1701** (2017) 032 [`1512.03918`].

[68] C. Bonvin, S. Andrianomena, D. Bacon, C. Clarkson, R. Maartens, T. Moloi et al., *Dipolar modulation in the size of galaxies: The effect of Doppler magnification*, *Mon. Not. Roy. Astron. Soc.* **472** (2017) 3936 [`1610.05946`].

[69] M. Borzyszkowski, D. Bertacca and C. Porciani, *LIGER: mock relativistic light-cones from Newtonian simulations*, *Mon. Not. Roy. Astron. Soc.* **471** (2017) 3899 [`1703.03407`].

[70] E. Giusarma, S. Alam, H. Zhu, R. A. C. Croft and S. Ho, *Relativistic asymmetries in the galaxy cross-correlation function*, `1709.07854`.

[71] S. Alam, H. Zhu, R. A. C. Croft, S. Ho, E. Giusarma and D. P. Schneider, *Relativistic distortions in the large-scale clustering of SDSS-III BOSS CMASS galaxies*, *Mon. Not. Roy. Astron. Soc.* **470** (2017) 2822 [`1709.07855`].

[72] S. Alam, R. A. C. Croft, S. Ho, H. Zhu and E. Giusarma, *Relativistic Effects on Galaxy Redshift Samples due to Target Selection*, *Mon. Not. Roy. Astron. Soc.* **471** (2017) 2077 [`1709.07856`].

[73] H. Zhu, S. Alam, R. A. C. Croft, S. Ho and E. Giusarma, *N-body simulations of gravitational redshifts and other relativistic distortions of galaxy clustering*, *Mon. Not. Roy. Astron. Soc.* **471** (2017) 2345 [`1709.07859`].

[74] M.-A. Breton, Y. Rasera, A. Taruya, O. Lacombe and S. Saga, *Imprints of relativistic effects on the asymmetry of the halo cross-correlation function: from linear to non-linear scales*, *Mon. Not. Roy. Astron. Soc.* **483** (2019) 2671 [`1803.04294`].

[75] D. B. Thomas, M. Bruni, K. Koyama, B. Li and G.-B. Zhao, *f(R) gravity on non-linear scales: The post-Friedmann expansion and the vector potential*, *JCAP* **1507** (2015) 051 [`1503.07204`].

[76] L. Reverberi and D. Daverio, `fRevolution` – *Relativistic Cosmological Simulations in* $f(R)$ *Gravity I: Methodology*, `1905.07345`.